Fluid Evolution at the Batu Hijau porphyry Cu-Au deposit, Indonesia: Hypogene Sulfide Precipitation at Low-Temperature from a Single-Phase Aqueous Magmatic Fluid during Chlorite-White Mica Alteration

Michael Schirra, Oscar Laurent, Tobias Zwyer, Thomas Driesner, Christoph Heinrich

Fluid Evolution at the Batu Hijau porphyry Cu-Au deposit, Indonesia: Hypogene Sulfide Precipitation at Low-Temperature from a Single-Phase Aqueous Magmatic Fluid during Chlorite – White Mica Alteration

Michael Schirra[1,*], Oscar Laurent[1,2], Tobias Zwyer[1], Thomas Driesner[1], and Christoph A. Heinrich[1,3]

[1]Institute of Geochemistry and Petrology, Department of Earth Sciences, ETH Zurich, 8092 Zurich, Switzerland

[2]CNRS, Géosciences Environnement Toulouse, Observatoire Midi-Pyrénées, F-31400 Toulouse, France

[3]Faculty of Mathematics and Natural Sciences, University of Zurich, 8093 Zurich, Switzerland

[*]email: michael.schirra@erdw.ethz.ch

Abstract

Mineralization at the Cu-Au porphyry deposit of Batu Hijau, Indonesia, was previously reported to be associated mainly within stockwork quartz veins associated with pervasive biotite-magnetite alteration. We use cathodoluminescence (CL) imaging of vein textures followed by microthermometry and LA-ICP-MS microanalysis of fluid inclusions to decipher the spatial-temporal evolution of the hydrothermal system. Our results indicate that sulfide precipitation largely postdated the main stockwork veining. Chalcopyrite and bornite were found in three textural positions: (1) within conspicuous quartz-poor veinlets ("paint veins") that post-date quartz stockwork veins and which also appear to account for the bulk of seemingly disseminated sulfides; (2) as centerlines in B-type veins; and (3) as interstitial grains in A-type veins. In all three textural positions, the sulfides occur together with a volumetrically minor, dull-luminescent quartz generation interstitially to the granular quartz dominating the stockwork veins. All three positions are associated with chlorite ± variable phengitic white mica with 3 – 6 wt.% FeO + MgO.

In the barren core of the deposit, quartz veins host, almost exclusively, fluid inclusions of intermediate density (~0.6 g/cm^3) and near-constant salinity of ~3.7 wt.% $NaCl_{eq.}$, representing the input magmatic fluid. This fluid subsequently separated into a highly saline brine[1] and low-density vapor during quartz vein formation in the mineralized parts of the deposit; however, we

[1] 'brine' is used here for a hypersaline liquid saturated with halite at room temperature and homogenizing to a liquid upon heating, 'intermediate density fluid' homogenizes near-critically by meniscus fading, whereas 'vapor inclusions' homogenize to vapor (Heinrich, 2005, tab. 2; Liebscher & Heinrich 2007).

found no textural or fluid-chemical evidence that brine + vapor already reached saturation in sulfides. Within the studied samples, Cu-Fe-sulfides are invariably associated with the dull-luminescent quartz hosting only low-salinity (~2 to 8 wt.% $NaCl_{eq}$) aqueous fluid inclusions with a density of ~0.8 g/cm^3 and minimum formation temperatures of 360° to 300°C, in agreement with Ti-in-quartz and chlorite thermometry indicating trapping conditions only slightly above the boiling pressure of these liquids. On average, this mineralizing aqueous fluid is compositionally similar to the initial magmatic fluid, suggesting a common source, but some inclusion assemblages deviate to significantly higher or lower salinities (25 and 0.5 wt.% $NaCl_{eq.}$, respectively).

We propose a formation model for the Batu Hijau porphyry Cu-Au deposit in which mostly barren quartz veins formed at high-temperature (> 400°C) in the central part of the system, while sulfide mineralization commences to form peripheral to this zone. The economic ore shell was growing in- and downwards as zones of active sulfide precipitation at 360°-300°C shifted in response to progressive retraction of isotherms, while barren quartz vein formation continued in the system's core at higher temperature. Some of the ore-forming aqueous liquid may have contracted directly from intermediate-density magmatic fluid, but the large salinity variations above and below the average are interpreted as evidence for re-homogenization of magmatic brine and vapor that had previously separated and became miscible again after cooling and contraction of the dominant former vapor. Retrograde solubility of quartz near 400°C and ~ 200 bar, which lead to partial dissolution of earlier formed quartz veins and created cavities and cracks for sulfide deposition. This evolution of a single magmatic fluid, with transient phase separation, but limited physical segregation of transient brine and vapor as they flow through the ore shell, may explain the observed positive correlation between ore grades and quartz vein density in the ore shell, even though sulfide precipitation overprints high-temperature quartz precipitation on the vein scale. A brief comparison with published observations indicates that this re-interpretation may apply to many other porphyry Cu-(Au-Mo) deposits worldwide.

Introduction

Porphyry-style deposits are major sources of Cu, Mo, and Au, and their magmatic-hydrothermal systems have been studied in detail over many decades (Sillitoe, 2010 and references therein). Early detailed mapping of porphyry deposits (e.g., Lowell and Guilbert, 1970;

Lowell, 1974; Gustafson and Hunt, 1975) led to similarities of porphyry systems being identified worldwide, indicating similar physicochemical conditions of ore formation (e.g., Henley and McNabb, 1978; Seedorff et al., 2005; Sillitoe, 2010). The deposits form around a central porphyritic stock or dike swarm, leading to a common sequence of veining associated with a coaxially arranged alteration pattern and a commonly bell-shaped ore body (e.g., Lowell and Guilbert, 1970) with a distinct temporal sequence of igneous and hydrothermal features (Gustafson and Hunt, 1975; Redmond and Einaudi, 2010; Sillitoe, 2010). Fluid inclusions within most porphyry-related hydrothermal quartz veins typically consist of two types, low-salinity vapor and high-salinity brine (Roedder, 1971, 1984; Nash, 1976; Cline and Bodnar, 1991; Bodnar, 1995; Landtwing et al., 2005; Redmond and Einaudi, 2010); these two coexisting fluids formed by separation of a single-phase magmatic fluid of low- to medium salinity (Henley and McNabb, 1978) commonly preserved as intermediate-density fluid inclusions in the deep core of the deposits (Redmond et al., 2004; Landtwing et al., 2005). High metal grades spatially correlate with potassic alteration and hydrothermal quartz veins hosting predominantly brine and vapor fluid inclusions (Gustafson and Hunt, 1975; Reynolds and Beane, 1985; Ulrich et al., 2002). This association of alteration, quartz veins and inclusion style, in combination with the truncation of mineralized quartz veins by the next younger porphyry intrusion (e.g., Gustafson and Hunt, 1975; Proffett, 2003), imply that at least some Cu-Fe-sulfide precipitation occurred during early quartz vein formation from a single-phase or two-phase fluid of highly saline brine coexisting with low-salinity vapor (Proffett, 2009; Sillitoe, 2010), probably at temperatures above 500° (Eastoe, 1978; Heithersay and Walshe, 1995; Harris et al., 2003; Proffett, 2003; Seedorff et al., 2005; Hezarkhani, 2009).

Cathodoluminescence imaging of porphyry quartz veins has become decisive to clarify the relationship between quartz vein formation and sulfide precipitation, and it indicates that quartz can be repeatedly dissolved and re-precipitated within veins of porphyry Cu deposits (Rusk and Reed, 2002). Detailed petrographic studies of several deposits with cathodoluminescence imaging have found evidence for similar episodes of quartz dissolution and precipitation over a large range of temperatures and pressures (Redmond et al. 2004; Landtwing and Pettke, 2005; Landtwing et al., 2005, 2010; Klemm et al., 2007; Müller et al., 2010; Vry et al., 2010; Stefanova et al., 2014; Gregory, 2017). In all cases studied so far, Cu-Fe sulfides are associated with a

volumetrically minor quartz generation, typically marked by distinctively low CL intensities. These studies imply that most sulfide precipitation occurred after the main mass of quartz vein formation at any one location, during or after partial quartz re-dissolution, from a fluid that was cooler than that which deposited the original quartz veins. Sulfide precipitation is commonly associated with re-opening of early veins, but the paragenetic sequence might be obscured if only macroscopic observations are taken into account. Evidence for high Cu-Fe sulfide solubility above 400°C (Crerar and Barnes, 1976; Hezarkhani et al., 1999; Liu and McPhail, 2005) and for a region of retrograde quartz solubility below approximately 1kbar (Fournier, 1983) are consistent with sulfide precipitation at low temperatures and pressures (Landtwing et al., 2010; Monecke et al., 2018). The aim of this paper is to use CL-petrography and fluid inclusion analysis to define the conditions and fluid state of Cu-Fe-sulfide precipitation at Batu Hijau, and to understand more generally the deposit-scale fluid evolution that leads to the — apparently conflicting but common — observation that a high density of early quartz veins coincides with high Cu grades deposited later in the paragenetic sequence.

Geological Framework

Batu Hijau is an Au-rich porphyry Cu deposit following the definitions of Sillitoe (1979; >0.4 g/t Au) and Kesler et al. (2002 ; Cu/Au <40,000), with total mineable reserves estimated at 914 Mt of ore averaging 0.525 wt.% Cu and 0.403 g/t Au (Clode et al., 1999). It is located in the southwestern corner of Sumbawa, an island within the E trending active intra-oceanic Sunda – Banda Arc in Indonesia (Fig. 1A). The Pliocene deposit lies at a major structural discontinuity cutting the arc, caused by the subduction of the Roo Rise, an oceanic plateau on the Indian Ocean plate (Garwin, 2000). Slab tearing due to subduction of the buoyant oceanic plateau is indicated by whole-rock geochemical and radiogenic isotope data, suggesting an asthenospheric mantle contribution to arc magmatism (Fiorentini and Garwin, 2010). This perturbation of the subduction zone is marked by a crustal-scale arc-transverse fault zone, which focused magma ascent and controlled the distribution of upper-crustal igneous activity (Garwin, 2002). The low K content of intrusive rocks in the vicinity of the mine area is consistent with rapid intrusion through thin oceanic crust approximately 14 to 23 km thick (Hamilton, 1979; Barbieri et al., 1987).

Batu Hijau is centered on a complex of pipe-shaped low-K calc-alkaline tonalite porphyritic intrusions, which intruded along the contact between gently westward-dipping volcaniclastic sequences of andesitic composition and a precursor equigranular quartz-diorite pluton (Fig. 1C; Meldrum et al., 1994; Garwin, 2000). The complex consists of three different porphyry intrusions; the mineralized and hydrothermally altered Old and Intermediate Tonalite are both crosscut by the Young Tonalite that is weakly mineralized and altered and post-dates the formation of economic ore grades (Clode et al., 1999). All tonalite intrusions consist of quartz, plagioclase, biotite, and hornblende phenocrysts in a fine-grained quartz – plagioclase matrix. The size and abundance of quartz phenocrysts increase from the Old to the Young Tonalite. Distinction between the Old Tonalite and the Intermediate Tonalite is only possible in a few places where the latter truncates quartz veins in the former, or by the presence of mineralized quartz vein xenoliths in the Intermediate Tonalite (Proffett, pers. commun., 1998). Due to the almost fresh appearance and much lower density of hydrothermal quartz veins, the relatively barren Young Tonalite is easy to distinguish from both mineralized porphyries (Fig. 2). Amphibole – plagioclase thermobarometry indicates minimum crystallization depths for phenocrysts of 8 km, significantly deeper than the emplacement depths of the tonalite porphyries at ≤ 2 km (Garwin, 2000). Recent chemical abrasion – isotope dilution – thermal ionization mass spectrometry (CA-ID-TIMS) U-Pb zircon dating of these intrusions indicate a maximum duration of the main hydrothermal mineralization of less than 90 ± 32 ky, bracketed by the emplacement of the three porphyries between 3.736 ± 0.023 Ma and 3.646 ± 0.022 Ma as determined by the youngest zircon grain from each sample (Large et al., 2020). Earlier U-Pb SHRIMP (Garwin, 2000) and LA-ICP-MS ages (Maryono et al., 2018) are consistent with these high-precision results.

Vein Sequence, Alteration and Mineralization

Distribution of hydrothermal mineralization, crosscutting relationships of various vein types and alteration patterns at Batu Hijau (Fig. 1, 2 and 3) are similar to other porphyry systems worldwide regarding spatial and temporal relationships (e.g., Gustafson and Hunt, 1975). Batu Hijau shows a regular concentric and vertical zonation of a high-grade ore shell overlying and surrounding a barren core. Veins and alteration types are categorized by Mitchell et al. (pers. commun., 1998) and Clode et al. (1999) into four types following the nomenclature of Gustafson

and Hunt (1975). Truncations of earlier quartz veins and sharp breaks in ore grade at intrusive contacts define timelines, indicating an early stage of bornite mineralization in some areas of the deposit (Setyandhaka et al., 2008); however, clear examples of such relations between the Old and Intermediate Tonalite were not encountered in the present study and have so far not been studied by CL-petrography. Here, we emphasize the importance of 'paint veins' (after Fournier, 1967), which are thin fractures coated by sulfides, truncating most quartz veins and intrusive contacts and presently hosting most of the ore associated with the earlier two porphyries. We focus on a N-S section through the deposit (Fig. 1C; mine data supplemented by own observations) and refer to three deposit parts as barren core (centered on the tonalite complexes at depths of 750 to 1200 m relative to the pre-mining surface), mineralized flanks (roughly following the margins of the tonalite complex surrounding the barren core) and the mineralized center (from the pre-mine surface to the top of the barren core). Observations were made during three visits in 2009 (Zwyer, 2010), 2016 and 2017, studying mine outcrops and 7 drill holes and taking more than 100 samples from which 62 thin or doubly-polished sections were cut. The following description is based on own observations of mineralogy and local timing relations in core, largely using the nomenclature of Fournier (1967) and Gustafson and Hunt (1975), and building on earlier observations by Mitchell et al. (pers. commun., 1998), Code et al. (1999), Arif and Baker (2004) and Setyandhaka et al. (2008). A summary description of the samples and main vein types is given in Table 1 and 2, respectively.

Quartz-dominated veins and biotite – magnetite alteration

The earliest veins are discontinuous, wavy, magnetite-dominated quartz veins with biotite-rich alteration envelopes, called Am-type veins (Fig. 3C and D). They are commonly crosscut by discontinuous and undulating thin veins consisting entirely of anhedral quartz (A veins, Fig. 3A) and less common B veins with parallel walls, a main fill of euhedral quartz crystals and a characteristic sulfide centerline (Fig. 3E). AB-type quartz veins are thicker and straighter than A veins but lack a centerline (Fig. 3B and D), with local crosscutting relationships always showing A veins cut by AB and finally B veins. From A to B veins the quartz grains change from granular and anhedral to euhedral shapes, growing from the wall-rock into open space, which was eventually filled by sulfides. Within all quartz-vein types, minor feldspar, magnetite, anhydrite, biotite, chlorite, and rutile, as well as bornite, chalcopyrite, pyrite and molybdenite can occur. Magnetite

is commonly enriched along the vein walls, indicating reopening of early Am veins. Open spaces within quartz veins are abundant to depths of up to 1000 m below the pre-mining surface and might be the result of anhydrite dissolution by ground water as purple anhydrite variably hydrated to gypsum is present in deeper parts of Batu Hijau. In general, A veins are the dominant vein type whereas B veins are minor but slightly increasing in abundance in the shallower parts of the deposit.

Biotite – magnetite alteration is associated with quartz-rich stockwork veins (type Am, A, AB and B) and characterized by pervasive replacement of primary mafic minerals by brown shreddy biotite and magnetite (Fig. 3G). Primary Ca-rich plagioclase (andesine to oligoclase) is partially replaced and overgrown by more Na-rich compositions (Clode et al., 1999). Hydrothermal K-feldspar is generally absent. Biotite – magnetite alteration assemblages are preserved in the barren core, where quartz vein densities are high but Cu-Fe sulfides are rare (Clode et al., 1999; Setyandhaka et al., 2008). The biotite – magnetite alteration zone grades outwards to a propylitic alteration zone, which is subdivided into an inner actinolite and an outer epidote-chlorite domain (Garwin, 2000; Wilkinson et al., 2015).

Veins and fractures with chlorite – white mica alteration

Chalcopyrite – bornite veinlets associated with feldspar-stable chlorite – white mica alteration envelopes, called C veins, are < 0.5 cm wide and rare compared to quartz-dominated vein types at Batu Hijau (Clode et al., 1999; Arif and Baker, 2004). By far more abundant are hairline fractures coated with chalcopyrite and minor bornite or pyrite, which can be inconspicuous in cut sample surfaces and appear as 'disseminated' sulfides (Fig. 2A and B). However, they are ubiquitous in the ore shell, as mineralized rocks almost invariably break during blasting or hammering along these greenish, sulfide-coated fractures. Because of this appearance on broken surfaces, we call them "paint veins" following Fournier (1967). Both, C veins and paint veins crosscut all quartz vein types, although actual timing relationships can be obscured by the presence of open spaces and the interruption of their thin alteration halo at intersections with unreactive vein quartz (e.g., Fig. 3B). Commonly, only a crack propagating through earlier quartz veins or a few aligned sulfide grains document the real time relationships. Paint veins can merge with the centerline infill of B veins, commonly introducing chlorite or white mica with sulfides into these veins and adjacent wall rock (Fig. 3L). Themselves they contain little or no quartz. Due to their similar timing and

mineralogy, both vein types have probably formed at similar times and conditions, with C veins just being thicker and more distinctly filled paint veins. Based on their mineralogy there appears to be a spectrum of paint veins ranging from bornite-dominated, chlorite-rich to chalcopyrite-dominated, white mica-rich versions. A sharp decrease in ore grade and drastic change in chlorite – white mica alteration intensity at intrusive contacts, and locally discernable truncations of paint veins (Fig. 2) indicate that they mostly pre-date the emplacement of the Young Tonalite, but there are also paint veins (as well as a few A-type quartz veins) postdating it. No sample material was available to establish timing relations at intrusive contacts between Old and Intermediate Tonalite. In general, paint vein truncations at intrusive contacts might be rarely visible due to the thin and porous appearance of those veins, which renders them more prone to be reworked by the infiltrating melt close to the contact. Conversely, paint veins might be re-opened during final cooling and extend into the younger intrusion. Although paint veins have been reported in previous studies as fracture coatings (Clode et al., 1999; Setyandhaka et al., 2008), their importance for Cu introduction has not been evaluated. The volumetric abundance of paint veins is difficult to determine but the characteristic pale-green color of broken ore (e.g., Fig. 2A), the ubiquitous presence of seemingly disseminated sulfides on planar surfaces down to cm-sized fragments and their connection to sulfide-filled centerlines and fractures in earlier quartz veins indicate that paint veins are in fact the predominant vein type in the ore shell in terms of vein surface per ore volume. The grade jumps at contacts of Young Tonalite indicate that they probably introduced most of the Cu-Fe-sulfide (chalcopyrite and bornite) present in the mineable ore.

Chlorite – white mica alteration with secondary albitic plagioclase is concentrated along C and paint veins (Fig. 3B, D and Fig. 4) and pervades the ore system, overprinting biotite – magnetite alteration (Fig. 1B and 4B). In the sample material used for this study hardly any completely unaltered biotite grain was observed, except in the barren core where paint veins appear to be less common. In addition to partial or complete replacement of biotite by chlorite and white mica, igneous Ca-rich plagioclase is altered to fine-grained intergrowths of white mica and calcite, whereas the Na-rich rims remain stable (Fig. 3H to J). Excess Ti and Ca, released from the breakdown of Ti-rich biotite and Ca-rich plagioclase, are fixed as rutile or anatase (Fig. 3K) and as calcite, epidote, apatite and anhydrite. In addition, titanite and barite are present, albeit rare, as

234 euhedral crystals in open spaces. Earlier magnetite was partially transformed to hematite along
235 internal fractures and grain boundaries.
236 *Pyrite-dominated veins and feldspar-destructive white mica – clay alteration*
237 Pyrite-dominated D veins are associated with distinct halos of white mica ± clay alteration
238 characterized by pervasive feldspar destruction (Fig. 3A and F). These veins crosscut all previously
239 formed vein types and can contain minor quartz and chalcopyrite in addition to pyrite. D-type
240 veins occur in all rock types and, in contrast to most previous veins, invariably cut across the
241 contacts to the Young Tonalite.
242 Clay alteration is characterized by the formation of smectite, white mica and minor chlorite
243 after feldspar destruction along base metal veins filled with sphalerite, galena, tennantite, pyrite
244 and minor amounts of chalcopyrite and bornite (Clode et al., 1999). Intense clay alteration only
245 occurs in a limited zone at the eastern top of the deposit (Maryono et al., 2018) and was not
246 studied here.
247 *Metal distribution*
248 The ore body has the shape of an inverted cup with a barren core in the deep center
249 surrounded by mineralized flanks (Fig. 1D and E). At the mine scale, the ore shell overlaps with
250 the biotite – magnetite alteration zone (Clode et al., 1999; Arif and Baker, 2004), which is variably
251 overprinted by chlorite – white mica alteration. At the resolution of mine blocks and blasthole
252 assays the ore shell is strikingly regular with generally decreasing ore grades with distance from
253 the intrusion center, excluding the weakly mineralized Young Tonalite. Sharply decreasing ore
254 grades at the contact from the Old Tonalite to the Intermediate Tonalite, are locally documented
255 by Setyandhaka et al. (2008), but are not generally recorded in the ore shell model of the
256 operating mine and could not be confirmed in this study due to the scarcity of samples where the
257 contact is clearly visible. Although Cu and Au both have similarly regular distribution patterns (Fig.
258 1D and E), the Cu/Au ratio varies systematically within the deposit (Fig. 1B), generally decreasing
259 with depth and laterally from the core to the periphery (Arif and Baker, 2004). The Young Tonalite
260 has ~10 times lower metal grades (typically < 0.3 wt.% Cu; Fig. 1D) and a significantly higher Cu/Au
261 ratio based on blasthole assays from the -30m level, documenting a weak late phase of
262 dominantly Cu introduction or dispersion. In general, Ag contents are atypically high in Batu Hijau
263 ore (up to 15 g/t) compared to other Au-rich porphyry deposits (<3 g/t; Sillitoe, 1997) and

correlate better with Cu grades than Au in the investigated drill holes. Economic amounts of molybdenum are absent in Batu Hijau and molybdenite was only encountered as small flakes within B-type quartz veins from the barren core.

Chalcopyrite and bornite are the main Cu-Fe sulfides, with minor amounts of digenite and chalcocite (Arif and Baker, 2004). Digenite and chalcocite intergrown with bornite is reported to only occur within A-type quartz veins and was therefore interpreted to represent an early low-sulfidation assemblage that was subsequently transformed to the higher sulfidation assemblages chalcopyrite – bornite and eventually chalcopyrite – pyrite (Clode et al., 1999). Native gold and electrum are typically attached to or enclosed in the Cu-Fe sulfides (Arif and Baker, 2004). Only a few µg/g of Au are present as homogenous solid solution within Cu-Fe sulfides (Kesler et al., 2002), which therefore cannot host the bulk of the Au ore grade. Cu-Fe sulfides are most conspicuous in quartz veins and Cu and Au grades are highest in areas of high quartz vein density, indicating that ore minerals are mostly hosted in A, AB and B veins (Clode et al., 1999; Arif and Baker, 2004; Setyandhaka et al., 2008). Sulfide grains in quartz veins are apparently randomly distributed, but even macroscopically are commonly seen to line up along small cracks, follow a centerline or cement open spaces between euhedral quartz crystals that grew into cavities. In the barren core, where vein densities are high, but Cu-Fe sulfides are either rare or absent, the lower ore grades do not correlate with the high vein density.

Sampling and Methods

Due to the regular concentric vein and ore distribution at Batu Hijau, sampling was conducted largely on one N-S section (000) covering the extent of mineral zonation (Fig. 1). We thereby missed an area in the Western part of the deposit where Setyandhaka et al. (2008) found high-grade ore with early bornite in A-veins hosted by Old Tonalite and truncated by Intermediate Tonalite, which we acknowledge as a possible bias of the present study. Petrographic observations, secondary electron microscope – cathodoluminescence (SEM-CL) imaging, fluid inclusion microthermometry, and laser ablation – inductively coupled plasma – mass spectrometry (LA-ICP-MS) analysis of fluid inclusion assemblages were carried out at ETH Zürich, focusing on 19 samples from five boreholes. In total, 27 thin (30 µm) and 35 double-polished thick (300 µm) sections were prepared for petrographic work and analysis.

We used SEM-CL imaging and conventional petrography of polished thin sections to document the textural relationships and sulfide distribution relative to quartz, and to determine fluid inclusion assemblages (FIAs) within quartz veins. Several thousand SEM-CL images were obtained using a JEOL JSM 6390 LA Secondary Electron Microscope equipped with a Deben Centaurus CL detector at an acceleration voltage of 15-kV. Spot size, and hence energy density, was adjusted according to the CL-intensity of quartz in the different vein types. Images were taken with 80x to 200x magnification, 60 s acquisition time and a resolution of 1280 x 960 pixels.

The same SEM device was used for spectral imaging and quantitative analysis of alteration minerals, using iSpectra (Liebske, 2015) to create phase maps based on X-ray spectral images obtained by energy-dispersive spectroscopy (EDS). Images were taken at 15-kV acceleration voltage, 20 minutes acquisition time, a magnification between 80x and 100x, and a resolution of 256 x 192 or 512 x 384 pixels, resulting in pixel sizes of approximately 10 or 5 μm. Quantitative EDS analyses of chlorite was conducted after calibration for Na, Mg, Al, Si, K, Ca, Ti, Mn and Fe at 15-kV acceleration voltage and dead times between 25 and 30%. The reported compositions are average values obtained by 5 to 15 point measurements per individual chlorite crystal.

For microthermometric measurements, chips were cut out of double-polished thick sections, with 1878 fluid inclusions in 339 FIAs analyzed by a Linkam THMSG 600 heating-freezing stage. Heating and freezing experiments were conducted on FIA as defined by Goldstein and Reynolds (1994) to avoid unrepresentative results from fluid inclusions that entrapped mixtures of fluids or were significantly modified after their formation. Timing of fluid entrapment relative to the growth of the host mineral is based on petrographic criteria, following Goldstein and Reynolds (1994). Synthetic fluid inclusions of known compositions were used for calibration of the heating-freezing stage within ±0.3°C at -56.6°C, ±0.05°C at the melting point of ice and ±2°C at 374.1°C, the critical point of pure water. Freezing experiments were conducted first to avoid decrepitation of lower-temperature fluid inclusions during heating runs. Microthermometric results were processed with HokieFlincs (Steele-MacInnis et al., 2012) based on Driesner and Heinrich (2007) to obtain minimum entrapment temperatures, salinities, and densities of entrapped fluids.

The chemical composition of 600 fluid inclusions from 105 FIAs were subsequently analyzed by LA-ICP-MS using the ETH-prototype Excimer 193 nm (ArF) laser ablation system coupled to a PerkinElmer NexION 2000, fast-scanning quadrupole ICP-MS. The sample introduction system,

including the in-house, fast-washout (ca. 6 cm^3) glass ablation cell, was cleaned to minimize contamination, following the recommendations of Schlöglová et al. (2017). We used a laser repetition rate of 10 Hz, energy density of ca. 15 to 20 J/cm^2 and spot size set as to entirely ablate the targeted inclusion (typically between 5 and 40 µm inclusion size at depths up to approximately 100 µm). A progressive spot diameter increase up to 40 µm was applied using an iris aperture whenever necessary, to prevent quartz cracking upon ablation (Pettke et al., 2012). The detailed procedure is described by Günther et al. (1998), Audétat et al. (1998) and Heinrich et al. (2003). Element quantification was based on external calibration to the NIST SRM610 glass reference material (Jochum et al., 2011) and to the Sca-17 scapolite reference material for S, Cl, and Br (Seo et al., 2011), both ablated with laser spot diameters of 40 µm and energy densities of ca. 5 J/cm^2. The SILLS software (Guillong et al., 2008a) was used for data reduction. Each time-integrated signal was first critically scrutinized for elemental peaks that clearly belong to the fluid inclusion signal, to avoid misinterpretation of the results with analytical artifacts such as spikes or matrix fluctuations. Absolute concentrations were calculated from measured element ratios using Na as internal standard, based on total salinities obtained by microthermometry (wt.% $NaCl_{eq.}$) corrected for the effects of other salts (Heinrich et al., 2003; Steele-MacInnis et al., 2016). This procedure possibly introduces systematic errors, so that the background-corrected element ratios were preferred here for data interpretation (e.g., Seo et al., 2009; Schlöglová, 2018). Ratios, concentrations, and their standard deviations (1σ) reported here are based on average values of typically 4-7 fluid inclusion analyses belonging to a common FIA. This procedure allows identification of outliers within a group of fluid inclusions that represent a common fluid according to petrographic observations and microthermometric measurements, and to assess analytical uncertainties including degrees of heterogeneous entrapment and post-entrapment modification (Pettke et al., 2012).

We also obtained trace element compositions of hydrothermal quartz by LA-ICP-MS, either directly from the matrix signals of fluid inclusion analyses (as implemented in SILLS; Guillong et al., 2008a) or from individual spot analyses along profiles through veins, using Si as internal standard for trace element quantification. In addition to elements monitored during fluid inclusion analysis, P, Ge and Ga were included in the elemental setup of trace element analysis of quartz.

353 Data obtained by microthermometry, LA-ICP-MS analysis of fluid inclusions and quartz as well
354 as SEM analysis of chlorite grains is available as electronic repository.

355 ## Results

356 *Cathodoluminescence of hydrothermal veins*

357 Based on CL-intensities and the inferred relative chronology of the different vein types (table
358 2), four major quartz generations, Q_1 to Q_4, can be differentiated. In general, the brightness of CL
359 images decreases from early A-vein quartz (Q_1) over AB (Q_2) and B (Q_3) veins to almost non-
360 luminescent paint-vein quartz (Q_4). Anhedral early A- and AB-vein quartz commonly shows
361 blurred zoning patterns, whereas euhedral quartz grains of B and paint veins show oscillatory
362 growth zoning. Early A-type quartz locally contains rutile needles. The second generation of
363 quartz (Q_2), characteristic of AB veins, has a slightly weaker luminescence intensity than A-type
364 quartz veins. The crystals are anhedral to subhedral and have diffusive or sharp growth zonation
365 (Fig. 5A). The third generation of quartz (Q_3), typical of B veins, is characterized by a medium gray
366 luminescence and euhedral growth zoning (Fig. 5B). The intensity of gray luminescence can vary
367 moderately between individual growth zones. Quartz crystals have commonly overgrown earlier
368 generations of quartz (Fig. 5B). The fourth generation of quartz (Q_4) has dull luminescence and
369 occurs either as filling of a network of micro-cracks that follow and crosscut grain boundaries and
370 growth zones of earlier generations, or as euhedral quartz grains growing into open spaces (Fig.
371 5B-D, 6 and 7). The transition between Q_4 and earlier Q_{1-3} is typically abrupt and irregular, caused
372 by quartz dissolution preferentially along crystal boundaries and micro-fractures prior to Q_4 re-
373 precipitation. Locally, straight grain boundaries show that euhedral bright-luminescent quartz
374 grains were overgrown by Q_4 without intervening quartz dissolution. Q_4 can contain fragments of
375 Q_{1-3} (e.g., Fig. 5A). Dull-luminescent Q_4 occurs within paint veins, within earlier veins at
376 intersections with paint veins (Fig. 5A) and along sulfide centerlines of B veins (Fig. 5B to D).

377 In all investigated samples, quartz vein-hosted sulfide grains, including bornite displaying
378 digenite exsolution lamellae, are systematically associated with a fracture network filled by Q_4
379 (Fig. 6). Sulfide grains are aligned along growth zones in Q_4 or were deposited over the newly
380 grown Q_4 grains (Fig. 7). Only a few bornite grains (<< 1% of all imaged sulfides) have been found
381 without any contact to Q_4 on the imaged surface (e.g., the small bornite grain in Fig. 6C) but even

these apparently isolated sulfide inclusions in earlier quartz generations appear to be associated with grain boundaries or cracks in the third dimension that are not visible by CL imaging of the sample surface. In addition to sulfides, Q_4 is spatially associated with, and contains inclusions of minerals typical for chlorite – white mica alteration associated with paint veins, i.e. chlorite, white mica, calcite, apatite, rutile, barite and anhydrite (Fig. 6, 7, 10C and 13). Based on luminescence, quartz from paint and D veins is not distinguishable and thus some of the quartz classified as Q_4 may have precipitated during D-vein formation.

Trace elements in hydrothermal quartz

Trace elements were analyzed along profiles through veins containing all quartz generations (Fig. 7C). Commonly detected elements are Li, B, Na, Mg, Al, K, Ti, and Ge, while other elements such as Cl, Ca, Fe, Cu, Sr, and Ag were rarely above detection limit, which may relate to silicate, sulfide or fluid inclusions.

In general, concentrations of Li, B, Al, and Ti have the largest systematic variations between different quartz generations (Fig. 8 and 9, table 3), while other trace elements like Na, Mg, P, and K have no systematic differences. With up to 100 µg/g for Na and K, these trace elements are high in all quartz generations compared to most other trace elements. From Q_1 to Q_4 Li, B, and Al systematically increase, whereas Ti shows the opposite trend (Fig. 8 and 9). However, discrimination of the different vein types based on trace element compositions is not straightforward since most element concentrations overlap. Titanium concentrations are highest in Q_1 and Q_2 (50 to 150 µg/g), consistent with the presence of thin rutile needles. In contrast, the Li, B, and Al concentrations in Q_1 and Q_2 are the lowest, 1 µg/g, 0.5 to 1 µg/g, and 100 µg/g, respectively. In Q_3, Ti contents (10 to 80 µg/g) are lower than Q_1 and Q_2, whereas Li and Al concentrations are higher but still show a significant overlap (respectively 2 and 22 µg/g on average). The average Ti concentrations in Q_4 (ca. 9 µg/g, with some values < 1 µg/g) are the lowest among all quartz types, whereas Li, B, and Al contents are the highest, reaching concentrations of 10 µg/g, 5 µg/g and a few thousand µg/g, respectively. Due to the appearance of Q_4 as thin cracks, spot sizes overlapped with the surrounding, earlier quartz resulting in a mixture of trace elements from different quartz generations that resulted in a wide range of Li, Al, and Ti concentrations (Fig. 9). The outliers of low Ti concentrations of cracks filled by Q_4 are lower than Ti concentrations in quartz-dominated veins but overlap with the concentration of Ti

412 in paint veins, indicating that mainly Q_4 was analyzed during these measurements. The two
413 outliers in AB veins with Ti concentrations below 10 µg/g, also reflect the presence of Q_4,
414 potentially due to ablation very close to euhedral dull-luminescent quartz, which could be
415 dominant at depth.

416 *Mineral thermometers*

417 Based on experiments above 600°C, Wark and Watson (2006) proposed that Ti concentrations
418 in quartz correlate with its formation temperature and developed a thermometer. This
419 thermometer was later recalibrated and corrected for the effect of pressure by Huang and
420 Audédat (2012), who also warned of overestimating precipitation temperatures due to high and
421 variable growth rates in hydrothermal environments. Based on the ubiquitous presence of rutile,
422 the activity of Ti was set to 1 (Wark and Watson, 2006). Pressures varied between 0.75 and 0.2
423 kbar depending on estimated depth and rock behavior during vein formation.

424 Applying the pressure-corrected formula of Huang and Audédat (2012), the Ti-in-quartz
425 temperatures range from 700°C in Q_1 to ~ 330°C in Q_4. In the barren core, high Ti concentrations
426 in Q_1 from A veins yield temperatures between 620° to 700°C, comparable with Ti-in-quartz
427 temperatures from early quartz veins in other porphyry systems (e.g., Rusk et al., 2008a; Müller
428 et al., 2010). Based on lower Ti contents, Q_2 in AB veins from the mineralized ore zone formed
429 between 550° and 650°C. Q_3 points to formation of B veins in a narrow temperature range
430 between 410° and 500°C, in agreement with the ductile-brittle transition region for porphyry
431 systems (Fournier, 1999). Low Ti concentrations in Q_4 indicate formation temperatures mostly
432 between 330° and 380°C.

433 Chlorite composition has been proposed as a geothermometer (McDowell and Elders, 1980;
434 Walshe, 1986; Cathelineau, 1988). We used the major element composition of hydrothermal
435 chlorite from the ore zone at Batu Hijau to calculate the temperature range of chlorite – white
436 mica alteration using the adjusted calibration of Jowett (1991), which considers the effect of Fe
437 and Mg on the temperature dependency of incorporation of tetrahedrally coordinated aluminum.
438 Following the suggestions of Inoue et al. (2010), chlorite with ($CaO + Na_2O + K_2O$) > 0.5 wt.% was
439 regarded as contaminated with other mineral phases such as white mica or calcite and were
440 therefore avoided. Most analyzed chlorites plot in the pycnochlorite and ripidolite fields (Hey,
441 1954). Iron numbers (FeO/FeO+MgO) are between 0.35 and 0.60 for chlorite replacing biotite

along paint veins and between 0.60 and 0.85 for chlorite rosettes within dull-luminescent quartz (Fig. 10A). Specifically, the rims of chlorite rosettes are Fe-rich and plot close to the daphnite field (Fig. 10). Tetrahedral silicon varies from 5.36 to 5.82 a.p.f.u. Electron microprobe analyses of chlorites from Batu Hijau by Mitchell et al. (pers. commun., 1998) and Wilkinson et al. (2015) overlap with our data (Fig. 10). Calculated temperatures range from 290° to 380°C with an average of 340°C. Applying the T-R^{2+}-Si diagram of Bourdelle and Cathelineau (2015), which is best at low temperatures (< 350 °C), low pressures (< 3-4 kbar) and assumes chlorite – quartz equilibrium (Inoue et al., 2009; Bourdelle et al., 2013), also yields mostly 300° to 350°C (Fig. 10B).

Fluid inclusion distribution and microthermometry

Four main fluid inclusion types were distinguished at Batu Hijau based on phase proportions at room temperature: intermediate density (ID: Fig. 11A), brine (B: Fig. 11C to F), vapor (V: Fig. 11B and F), and aqueous (AQ: Fig. 11G to J) fluid inclusions. Vapor, ID and AQ inclusions are two-phase fluid inclusions, distinguished by bubble sizes of 70-95 (V), 35-70 (ID) and 10-35 vol.% (AQ). Most ID and V inclusions have negative-crystal shapes, and many contain small opaque daughter crystals with tetragonal shapes, thought to be chalcopyrite. In contrast, AQ inclusions are typically more rounded or irregular in shape and rarely contain solids. Brine inclusions contain up to 7 different crystals; cubic halite and opaque crystals are always present, and sylvite, hematite, and either anhydrite or calcite are common. Liquid CO_2 at room temperature and clathrate melting during freezing experiments was not observed in any fluid inclusion type.

Most FIA are of secondary origin, and any rare ID, B, and V inclusions on clear growth zones are mostly too small for further investigations (≤ 1 μm) with a few exceptions (e.g., Fig. 11J). Microthermometry results are shown in Figure 12.

ID inclusions are dominant in A, AB, and B veins of the barren core of the deposit but are rare to absent at depths shallower than around 800 m below the pre-mining surface (Fig. 1C). They typically form secondary FIAs along fracture planes within Q_1 to Q_3 and homogenize by meniscus fading (critical behavior) at temperatures between 370° and 390°C in A-veins and 340° to 370°C in B-veins. Ice melting over a narrow temperature range between -2.4° to -2.1°C yields a constant salinity of around 3.7 wt.% $NaCl_{eq.}$ for all ID inclusions (Fig. 12). Calculated densities of ID inclusions range from 0.55 to 0.65 g/cm^3.

The V and B inclusions dominate in vein quartz from the ore shell of the deposit (Fig. 1C). Due to the clustering of inclusions, distinguishing individual FIAs is difficult. All B and V assemblages are therefore characterized as secondary inclusions relative to their bright-luminescent host quartz (mainly Q_2 and Q_3). The apparent disappearance of the last liquid in V inclusions is assumed to be generally well below homogenization temperature (Sterner, 1992). Final ice melting in V inclusions was only occasionally observable and yielded total salinities between < 1 to > 10 wt.% $NaCl_{eq}$.

The B inclusions are separated into three subgroups. Subtype 1 (B_1, Fig. 11C) is rare and dominantly occurs in the barren core, characterized by a small halite crystal (30 to 35 wt.% $NaCl_{eq.}$) and a bubble of approximately the same size as the halite crystal (10 to 20 vol.%). Inclusions of this type always homogenize by bubble disappearance to the liquid at temperatures of ~ 320°C. Subtype 2 (B_2, Fig. 11D) is more abundant and describes B inclusions with larger bubbles (20 to 30 Vol.%) and higher salinities (35 to 45 wt.% $NaCl_{eq.}$), usually with a small opaque crystal, thought to be chalcopyrite, and rarely hematite, sylvite or anhydrite. Like subtype 1, homogenization is always to the liquid at temperatures between 350° and 500°C by bubble disappearance. Subtype 3 (B_3, Fig. 11E) describes B inclusions with up to seven crystals present and small bubble volumes (~ 20 vol.%). Apart from halite and chalcopyrite that are identified in all inclusions, hematite, sylvite, and anhydrite are variably present. Ryan et al. (2001) identified other Ca, Sr, and Ba-bearing daughter crystals within poly-phase B inclusions from Batu Hijau using a nuclear microprobe. Inclusions of subtype 3 always homogenize by halite dissolution after bubble disappearance, yielding high salinities of > 50 wt.% $NaCl_{eq.}$. The temperature difference between halite dissolution and bubble disappearance in B_3 inclusions is 65°C on average. Overall, the salinity measured in B inclusions and the amount of daughter crystals increase with decreasing depth, from 900 m (on average 34.2 wt.% $NaCl_{eq.}$) to 300 m (on average 47.5 wt.% $NaCl_{eq.}$) below the pre-mining surface (Fig. 1C). Fluid inclusions trails that host B and V inclusions (Fig. 11F) are common and called “boiling trails”.

The AQ inclusions are typically small (< 5 to 10 µm) and occur throughout the deposit (Fig. 1C). They are the only inclusion type that occur in Q_4-filled cracks that cut earlier quartz veins and euhedral Q_4 grains that grew into open spaces (Fig. 13). In addition, rectangular AQ inclusions are also present in anhydrite within D-type veins (Fig. 11H). Homogenization temperatures, salinities,

and inclusion shapes allow the distinction of three inclusion subtypes: medium-salinity high-temperature (AQ_1), low-salinity high-temperature (AQ_2), and low-salinity low-temperature (AQ_3). The AQ_1 inclusions are rare and undistinguishable from AQ_2 inclusions at room temperature. During freezing experiments, hydrohalite or ice melting at -25° to -17°C indicate salinities of 20 to 25 wt.% $NaCl_{eq.}$ in AQ_1 inclusions. In AQ_2 inclusions, ice melting temperatures between -5.0° to -0.4°C indicate lower salinities of 0.7 to 8 wt.% $NaCl_{eq.}$. Typically, AQ_1 inclusions occur as primary or pseudosecondary FIA within the cores of euhedral Q_4, whereas AQ_2 inclusions are present as pseudo- or secondary trails within the outer rims of these crystals or Q_4-filled cracks terminated by sulfide grains (Fig. 13). Homogenization temperatures for both subtypes AQ_1 and AQ_2 range from 290° to 390°C, with an average of 324°C. In contrast to the rounded-shaped AQ_1 and AQ_2 FI subtypes, AQ_3 inclusions are flat and irregular in quartz (Fig. 11I) or rectangular in anhydrite (Fig. 11H) and usually occur within D veins. Ice melting temperatures vary between -3.0 to -1.0°C indicating salinities between 1 and 5 wt.% $NaCl_{eq.}$ with homogenization temperatures between 230° and 300°C.

Chemical composition of inclusion fluids

Elemental mass ratios to Na of analyses of 625 individual fluid inclusions within 107 FIAs are plotted as box plot diagrams for comparison between different fluid inclusion types (Fig. 14). Average concentration ratios, the second and third quartile (bottom and top of boxes, Fig. 14, respectively), and average concentrations of the different fluid inclusion types are reported in table 4. All values are based on averages of FIAs. Element ranges for all FIAs are interpreted to represent variations of the natural fluid compositions rather than analytical uncertainties.

In all types of fluid inclusions K, Fe, and S are the most abundant elements besides Na. Copper ratios to Na are high in ID, B, and V FIAs. However, Cu concentrations in ID and V inclusions are known to significantly exceed original Cu contents of the fluids due to post-entrapment modifications by coupled exchange of H^+ and Cu^+ between the inclusion and the ambient fluid, facilitated by excess S in the inclusions (Zajacz et al., 2009; Lerchbaumer and Audétat, 2012; Seo and Heinrich, 2013). Other elements are minor except for Mn with ratios relative to Na as high as 0.69 in some B FIAs. In general, K/Na, Rb/Na, and Cs/Na are uniform among all fluid inclusion types (overall average 0.42, 0.02 and 0.0005, respectively), whereas most other elements for the ID, B, and V FIAs have different ratios relative to Na. Metal/Na mass ratios in brine inclusions for

example are higher than in vapor inclusions. Intermediate density and AQ FIAs overlap with respect to all element ratios except for Cu/Na.

The ID inclusions contain all elements detected in other fluid inclusion types, with the composition of ID FIAs having values intermediate between B and V FIAs compositions. The highest concentrations in ID inclusions are S and Cu, with average S/Na of 2.4 and Cu/Na of 1.2. Average ratios of K and Fe to Na are 0.25 and 0.3, respectively, making them the second most abundant elements found in ID inclusions, followed by minor concentrations of Li, B, Mg, Mn, Zn and Ba with ratios to Na below 0.1, and As, Rb, Sr, Mo, Ag and Pb with ratios to Na below 0.01. The least abundant, yet frequently detected element is Cs, with an average Cs/Na ratio of 0.0006. Gold was rarely above the detection limit and locally detected values are interpreted to be either unidentified analytical artifacts (spikes) or tiny gold particles within the ablated inclusions.

Element mass ratios to Na in B and V FIAs are generally distinct from ID-type fluid compositions with Li, B, Cu, As, and Ag enriched in V inclusions and Mn, Fe, Zn, and Pb enriched in B inclusions relative to Na (Fig. 14). Exceptions are K, Rb, Sr, and Cs ratios to Na, which are comparable in B and V inclusions and overlap with those in ID inclusions. Because base metals, except Cu, were not part of the elemental setup for V inclusion analysis, direct comparison with V inclusions is not possible. Concentrations of all other measured element ratios in V inclusions are comparable to those in ID fluid inclusions. Compositions of V inclusions can be contaminated by the accidental entrapment of disproportionate amounts of brine as the wetting phase (Bodnar et al., 1985). Therefore, mass balance calculations following the procedure described by Klemm et al. (2007) and Landtwing et al. (2010) were used to obtain the original vapor composition (Table 5). Corrected element to Na ratios for V inclusions are shown as smaller boxes partially overlapping with analyzed element ratios for V inclusions in Figure 14.

The AQ inclusion compositions overlap with the ID fluid inclusions in most element ratios. The exception is Cu/Na that, which is more than an order of magnitude lower (mostly between 0.01 and 0.06) than in ID inclusions (mostly > 1). Although a small sulfur peak was commonly present in the time-integrated signals, usually S was below the detection limit because of the high and fluctuating S signal intensity during quartz ablation (Guillong et al., 2008b). AQ inclusions from D veins were too small to be analyzed.

Discussion

Batu Hijau, with its apparently predominant biotite alteration and dense quartz veining with bornite, chalcopyrite and gold grains, has been described as a pristine porphyry deposit that was not widely overprinted by feldspar-destructive alteration postdating ore formation. Our observations confirm this for silicate alteration and quartz veining, but we find that metal precipitation was mostly associated with chlorite – white mica alteration and decoupled from most of the quartz deposition, and occurred at significantly lower temperature, as summarized in Figure 15. The following discussion aims at linking vein-scale textural evolution and deposit-scale zonation with successive fluid inclusion generations. We argue that the present-day make-up of the deposit was dominated by an evolving fluid evolution path across a steep gradient in pressure and temperature in the outermost parts of a magmatic fluid plume, sourced by a cooling, subjacent, fluid-producing magma reservoir. The strong gradients developed in response to the formation of an interface between the hot magmatic fluid plume and externally convecting meteoric water as suggested by the numerical modelling of Weis et al. (2012). As a result, the fluid evolution path changed through time (Fig. 16), from an early prograde stage establishing the magmatic fluid plume to a retrograde stage of gradual magmatic fluid plume retraction, during which much, if not most, of the metals were introduced.

Vein-forming conditions and fluid evolution in space and time

Reconstructing the conditions of hydrothermal quartz vein formation based on fluid inclusions requires estimating temperature as well as pressure. The physical state of the magmatic fluid provides an estimate of the minimum pressure within the barren core at the time of A vein formation. The solvus of the ID fluid considering the binary H_2O-NaCl system at formation temperatures of early quartz veins (~ 500°C or more; Fig. 12, 15A) requires a minimum pressure of 0.69 kbar, corresponding to a depth of ca. 2.5 km based on lithostatic conditions, consistent with the partly ductile deformation of A veins (Fournier, 1999). Minor CO_2 of less than 2 mol% (the maximum based on lack of evidence for CO_2 phases in ID inclusions; Collins, 1979; Rosso and Bodnar, 1995) would shift the two-phase boundary to slightly higher pressures of approximately 0.75 to 0.8 kbar (Gehrig et al., 1986). The depth estimate agrees well with the geologically reconstructed depth of 2 ± 0.5 km for the top of the Young Tonalite (Garwin, 2000), indicating

589 that the exposed orebody extended from ≥ 1.5 to ≥ 2.5 km below the paleosurface at the time of
590 ore formation.

591 By contrast, the highest pressure indicated by boiling assemblages, i.e., fluid inclusions
592 entrapped along the two-phase curve in the H_2O-NaCl system model (Roedder and Bodnar, 1980),
593 is ~0.42 kbar in AB veins from the lower parts of the mineralized center (SBD 21 468m,
594 approximately 500 m below the pre-mining surface), corresponding to a lower fluid pressure than
595 lithostatic. Other boiling assemblages (excluding those homogenizing by halite disappearance,
596 which probably suffered post-entrapment H_2O loss; Audétat and Günther, 1999; Becker et al.,
597 2008; Lecumberri-Sanchez et al., 2012) yield even lower pressures between 0.25 and 0.10 kbar
598 (Fig. 12), indicating significant pressure variations during quartz vein formation, consistent with
599 expansion and transition of a single-phase fluid initially at lithostatic conditions to a vapor phase
600 condensing out a minor amount of brine at low pressures approaching hydrostatic or even
601 vaporstatic conditions. Such a range of rather low fluid pressures is typical for Au-rich porphyry
602 Cu deposits (e.g., Panguna: Eastoe, 1978; Grasberg: Weiland and Cloos, 1996; Far Southeast:
603 Hedenquist et al., 1998; Bingham Canyon: Redmond et al., 2004; Landtwing et al., 2005).
604 Murakami et al. (2010) and Landtwing et al. (2010) proposed that this observation indicates rapid
605 decompression in a hot fluid plume at this stage of quartz vein evolution and suggest co-
606 precipitation of both metals as a reason for the Au-rich nature of these porphyry Cu deposits.

607 *Quartz veins in the barren core* formed from a single-phase magmatic fluid as indicated by ID
608 inclusions as the dominant inclusion type (Fig. 1C). Pressure-corrected homogenization
609 temperatures suggest formation temperatures for A veins of approximately 450-510°C (Fig. 12).
610 Brine assemblages in A veins from the barren core are rare, show the lowest homogenization
611 temperatures of this inclusion type (300-330°C) and do not occur as boiling pairs (Fig. 12). Due to
612 the steepness of brine isochores, any pressure correction is small so that these brines must have
613 been significantly cooler than the earlier ID fluids in A veins of the barren core (< 370°C at 0.7 kbar
614 but more likely < 340°C at a hydrostatic pressure of ~ 0.3 kbar). Likewise, the straight B veins in
615 the barren core, suggesting more brittle rock conditions, formed close to hydrostatic pressures,
616 and pressure-corrected homogenization temperatures of ID inclusions are between 390° and
617 460°C. In summary, the fluid inclusions of the barren core show most clearly that successive fluids

618 record decreasing pressures from lithostatic to hydrostatic pressures and thereby cooled from >
619 510°C to ~ 300°C.

620 *Quartz veins in the ore shell* formed during phase separation of the ascending magmatic fluid,
621 as documented by boiling trails in AB and B veins. Co-existence of hypersaline liquid and low-
622 density vapor implies entrapment along the two-phase boundary, which means that measured
623 homogenization temperature and pressure are equal to the original entrapment conditions
624 (Roedder and Bodnar, 1980). In the mineralized center, these assemblages record mostly higher
625 temperature and higher salinity in the brines, implying a larger degree of phase separation
626 compared to boiling trails in the mineralized flanks (Fig. 12). Mass balance based on conservation
627 of H_2O and NaCl shows that a ID fluid that initially contained 4 wt.% NaCl can split into vapor with
628 1 wt.% NaCl and brine with 40 wt.% NaCl at a weight proportion of approximately 92% to 8%
629 (Table 5), showing that the vapor phase dominated by weight (and even more so by volume)
630 during AB and B vein formation, as argued for other shallow porphyry systems (Henley and
631 McNabb, 1978; Hedenquist and Lowenstern, 1994; Hedenquist et al., 1998; Williams-Jones and
632 Heinrich, 2005; Seo et al., 2009; Landtwing et al., 2010; Weis et al., 2012). The assumed salinity
633 of the vapor phase co-existing with a hypersaline liquid was calculated using the SoWat software
634 (Driesner and Heinrich, 2007) and corresponds to the maximum salinity expected upon phase
635 separation at pressures of 0.15 to 0.25 kbar. Higher salinities of up to 10 wt.% $NaCl_{eq.}$ in V FIAs
636 are probably the result of small amounts of co-existing hypersaline liquid that was coincidentally
637 entrapped resulting in erroneously high salinities (Roedder, 1984; Bodnar et al., 1985). Vapor
638 dominance is further supported by the chemical composition of the vapor, which is similar to that
639 of the intermediate density fluid implying condensation of a minor amount of brine from the
640 dominating vapor. Highest temperatures obtained from boiling assemblages in AB veins are 530
641 ± 10°C, while the lower range overlaps with those of B veins at 410 to 360°C (Fig. 12). Similar
642 formation temperatures of both vein types might derive from secondary boiling assemblages
643 trapped in AB veins during B-vein formation. The Ti-in-quartz thermometer yields slightly higher
644 formation temperatures for Q_2 and Q_3 between 600° to 500°C and 450° to 400°C, respectively.
645 Entrapment pressures from boiling assemblages in B veins vary between 0.13 and 0.18 kbar,
646 indicating a hydrostatic to vapor-static pressure regime (Fournier, 1999). Subsequent cooling of
647 the vapor phase below ~400°C led to a continuous increase of its density and resulted in partial

dissolution of previously formed quartz veins (Fournier, 1983), creating secondary pore space for subsequent fluid flow.

Paint vein formation and Cu-Fe sulfide precipitation occurred during and after partial re-dissolution of the dominant vein quartz at any one point in the deposit. Minor Q_4 quartz associated with paint veins and filling micro-fractures in earlier quartz veins exclusively host single-phase AQ inclusions (e.g., Fig. 13). Overlap between homogenization temperatures of 310 - 360° (Fig. 12), chlorite and Ti-in-quartz thermometry (290 - 410°C, Fig. 10) and the destruction of biotite to muscovite + chlorite indicate that the AQ FIs associated with paint vein formation in this temperature range require no significant pressure correction. The indicated temperature range also agrees well with the low concentrations of Au within bornite and chalcopyrite, suggesting precipitation temperatures of approximately 300°C at Batu Hijau (Simon et al., 2000; Kesler et al., 2002) and includes the pressure-temperature window of retrograde quartz solubility (400° to 350°C at 0.2 kbar; Fournier, 1999; Monecke et al., 2018) that precedes sulfide precipitation. The salinity of the AQ inclusions overlaps with the single-phase ID inclusions (3.7 ± 0.5 wt% $NaCl_{eq}$) but extends to notably lower as well as higher salinities (0.5 - 23.5 wt% $NaCl_{eq}$; Fig. 12). This large salinity range of the AQ fluid inclusions contrasts with most element ratios that largely overlap with those of the ID fluids of the barren core within less than one order of magnitude, with the exception of the significantly lower Cu content of the paint vein inclusions (Fig. 14). We therefore suggest that the paint vein-forming AQ fluid was derived from re-homogenization of brine and vapor phases from which the earlier quartz-dominated vein types formed, as explained in the next subsection. The intermediate saline AQ_1 inclusions can occur as primary FIAs in the cores of euhedral Q_4 (e.g., inset of Fig. 13 referring to Fig. 11J), indicating that Q_4 precipitation was initiated with the re-homogenization of brine with increasing amounts of contracting vapor.

The formation of D veins mostly post-dates the emplacement of the Young Tonalite (Fig. 15). Quartz- and anhydrite-hosted AQ FIAs indicate temperatures between 300° and 220°C (Fig. 12). The transition from paint to D veins might have been gradual based on the alteration mineralogy associated with these veins that progresses from chlorite – white mica over white mica – chlorite to feldspar-destructive white mica – clay alteration, suggesting increasingly reactive fluids with decreasing temperatures.

Changing fluid evolution during a downward-retracting mineralization front

On the scale of individual quartz veins, precipitation of Cu-Fe sulfides post-dates the main quartz vein event (Fig. 5, 6, 7 and 13). However, on the deposit scale, hydrothermal quartz and sulfides both precipitated from a common magmatic fluid, mostly at overlapping times but spatially separated under different physical conditions in different parts of the system. The main mass of vein quartz formed at higher temperatures, within the core of the magmatic fluid plume, while sulfides predominantly precipitated in the peripheral and shallower parts of the magmatic fluid plume where steep temperature and pressure gradients occurred in response to cooling effects of convecting meteoric fluids (Weis et al., 2012). As the magmatic fluid production gradually decreased with the progressive cooling of the magma reservoir, the magmatic fluid plume gradually retracted and, accordingly, zones of sulfide precipitation shifted in- and downward and overprinted the previously precipitated high-temperature quartz veins. This mine-scale evolution of the hydrothermal system (Fig. 16) can therefore be explained by three stages: 1) A prograde stage in which volcanic rocks are heated by a magmatic fluid plume until the maximum temperature and spatial extent of the hydrothermal system is reached; 2) a retrograde stage of sustained fluid flow through inward and downward retracting mineral precipitation fronts; and 3) a waning stage marked by an evolution path of magmatic fluids at overall lower temperatures at all depths.

The prograde stage (Fig. 16A) is characterized by the outward expansion of isotherms as the surrounding rocks are heated up by the porphyry intrusion and by the displacement of cold meteoric water by a focused magmatic fluid plume. Initial vein and alteration types form depending on P-T conditions. A-type quartz veins and biotite – magnetite alteration develop in the region of the present ore deposit around the top of the tonalite complex (~ 2 km paleodepth). Early bornite within A-type veins, as described by Clode et al. (1999), may precipitate due to rapid cooling of hot fluid against initially cold rock (e.g., McInnes et al., 2005). The observation by Setyandhaka et al. (2008) that such potentially early, high-grade bornite ore is mainly restricted to marginal relicts of Old Tonalite, supports such a quenching mechanism (Proffett, pers. commun., 2020). However, due to the high specific heat content of the fluid phase in combination with the focused fluid flux, the host rock heats up quickly to reach thermal equilibrium with the fluid phase, which may prevent further sulfide precipitation from the high-temperature magmatic

fluid. The total quantity of this early bornite mineralization is unknown as textural studies with CL-petrography are still lacking but likely to be minor, even though it may be of high grade locally. Once the host rock has been heated up to > 500°C, quartz may still precipitate due to gradual cooling and phase separation of the ascending magmatic fluid, contributing to A and AB vein formation. At near-hydrostatic pressures and temperatures of approximately 0.25 kbar and 450°C, phase separation produces a low-density vapor and a highly saline brine phase close to the vapor-liquid-halite surface in the salt – water system, which could explain the generally higher salinity B FIAs within shallower quartz veins (Fig. 1C; Fig. 12). However, most of the contained Cu, Fe and S was dispersed into the low-grade halo around the present deposit, where these components may have partly precipitated in early paint veins.

The retrograde stage dominated the development of the present-day ore shell (Fig. 16B) and reflects the downward retreat of isotherms due to overall cooling of the subjacent intrusive complex, leading to decreasing magmatic fluid production at progressively greater depth (Williams-Jones and Heinrich et al., 2005; Lamy-Chappuis et al, 2020). The resulting gradual thermal retraction of the hydrothermal system ('telescoping') could be triggered by syn-hydrothermal erosion or collapse of an overlying volcanic edifice (Sillitoe, 1994), but is a natural consequence of the generation of a stable interface between the hot magmatic fluid plume and hydrologically separated ground water convection cells (Fournier, 1999; Weis et al., 2012; Weis, 2015). During this hydrologically stabilized stage isotherms moved inward only slowly while the bulk of available magmatic fluid evolved along a path shown in Figure 16B, based on the inclusion record summarized in the lower part of Figure 15. Except for somewhat reduced brine salinity produced by phase separation at greater pressure, this fluid evolution path is the same as in the prograde stage (Fig. 16A). In the region of the hot barren core, ID fluids injected form below separated into brine and vapor, contributing additional barren A and AB type quartz. Although brine and vapor are both expelled from the lithostatically-pressured core and flow outward together, we speculate that the vastly different wetting properties and viscosities of the two fluid phases and the locally different but fast flow rates in narrow veins could prevent the two fluids from staying in chemical equilibrium at all times and locations in the complex vein network. As sulfur species (H_2S, SO_2) are preferentially enriched in the vapor while metals (Cu, Fe) are mainly transported in the brine (e.g., Drummond and Ohmoto, 1985; Pokrovski et al., 2005; Lerchbaumer

and Audétat, 2012; Zajacz et al., 2017), any small-scale isolation of the fluids will inhibit precipitation of Cu-Fe-sulfides and thus help maintaining high concentrations of these components in the respective fluids. As the two fluids flow outward into the hydrological contact region, they both cool below the critical temperature at hydrostatic pressures ($\lesssim$ 370°C at ~ 0.2kbar, Fig. 16B). As a result, the initially immiscible vapor contracts to a low-salinity aqueous liquid (Heinrich, 2005; Driesner and Heinrich, 2007) and becomes miscible again with the brine. This re-homogenization can explain the observation that the dominant aqueous fluid inclusions in paint veins have overall similar salinity and metal ratios as the original magmatic intermediate-density fluid inclusions (see Fig. 12 and 14), but with a greater salinity spread towards either side of 4 wt.% NaCleq., i.e. FIAs with lower salinity would be dominated by contracted vapor, whereas those with higher salinities up to 25% wt.% $NaCl_{eq.}$ originated by a locally greater admixture of brine. Transient physical isolation of brine and vapor in the barren core, followed by re-homogenization at lower temperature, will lead to re-combination of reduced sulfur and ore metals, which may explain the precipitation of most sulfides in paint veins and related cracks cutting earlier quartz stockwork veins. This idea, although difficult to prove quantitatively, can explain why Cu deposition was hampered during quartz vein formation and why it mainly precipitated at relatively low temperatures from a low-salinity, presumably H_2S-rich fluid. The range of Cu concentrations analyzed in AQ FIAs (~ 0.01 to 0.21 wt.%) are in good agreement with the modelled compositional range of primary fluids exsolved from calc-alkaline magmas (0.02 to 0.21 wt.% Cu, Chelle-Michou et al., 2017), concentrations of presumably non-modified ID-type fluid inclusions (0.01 to 0.05 wt.% Cu, Fiedrich et al., 2020) and overlap with the lowest concentrations found in ID FIAs from Batu Hijau (Fig. 14), indicating that no significant loss of Cu from the fluid occurred during its previous evolution. This is in line with the textural observation that many AQ FIAs appear to immediately pre-date Cu-Fe sulfide precipitation (Fig. 13). The limiting element for ore formation was Cu, as both, Fe and S, are present in higher quantities (up to 2 wt.%, respectively in AQ FIAs, although S was rarely quantifiable). Chemical transport and mineral precipitation is dominated by magmatic fluids, but in the absence of stable isotope data for Batu Hijau, minor input of low-salinity meteoric liquid cannot be excluded (cf. Fekete et al., 2018).

The waning stage (Fig. 16C) is marked by a fluid evolution path through an overall cooler system where the ductile to brittle transition shifted to even greater depth. Within the barren core at ~ 3 km paleo-depth, phase separation was suppressed at lower temperatures (< 450°C). The general absence of B and V inclusions in B veins within the barren core, but dominance of ID inclusions, indicate B vein formation from a single-phase fluid. The straight-walled B veins suggest formation during the waning stage under brittle conditions with no ductile deformation after emplacement. Compositionally, the B vein-hosted ID fluid inclusions are identical to those from earlier A-type veins, except for lower K/Na ratios. The similarity in fluid composition and the continuous fractionation of the inferred source magma indicated by falling temperature and evolving trace element composition of progressively younger zircons from the Old Tonalite to the Young Tonalite (Large et al., 2020) exclude major changes in the composition of the degassing magma chamber and the input fluid. Retrograde quartz dissolution did not occur anymore at the present mine level and dull-luminescent precipitated directly from an intermediate density fluid upon cooling, as indicated by continuous growth zoning from euhedral Q_3 to oscillatory zoned Q_4 (Fig. 13). Some chalcopyrite probably still precipitates during the waning stage but the major part of the present-day ore shell was completed during the retrograde stage.

The relative importance of the three stages for mineral precipitation cannot be quantified because of the difficulty of assigning veins to the Old and Intermediate Tonalite and the likelihood that veins of the older intrusion were reworked by the later intrusion and its fluid plume. We also do not know whether and to what degree a cycle of these stages already occurred between the emplacement of the Old and Intermediate Tonalite (Fig. 15, top). Nevertheless, the ubiquitous observation of quartz dissolution and re-precipitation prior to sulfide precipitation suggests that a greater proportion of vein quartz in the ore shell was formed in the prograde stage, whereas the bulk of the economic sulfide ore surrounding the present barren core formed during the retrograde stage of the hydrothermal system. This mainly occurred after emplacement of the Intermediate Tonalite but before the Young Tonalite, which was followed by a much weaker cycle of sparse A-type and paint veins.

The duration and total fluid quantities involved in these stages can be estimated from the rates of fluid production and expulsion simulated numerically for a magma chamber of suitable size for the formation of Batu Hijau. Assuming a parental magma containing 5 wt.% H_2O and an extraction

efficiency of ~ 50% (Chelle-Michou et al., 2017) of an ID fluid with ~ 2000 µg/g Cu (~ maximum Cu concentration detected in AQ FIAs), about 40 km^3 of source magma are required to generate Batu Hijau. These dimensions are similar to parameters used by Weis (2015) to model fluid flow through a generic porphyry deposit and by Lamy-Chappuis et al. (2020) to simulate its extraction rate from an upper-crustal magma chamber. The latter study predicts ~ 80 ky of focused fluid flow collected from an upper-crustal intrusion of this size. During the first ~ 20 ky the model predicts an advance of the 350 – 450°C isotherms, followed by more than 60 ky of steady state and slowly retracting isotherms while the largest fraction of available fluid is expelled. The total duration of this magma-chamber process is similar to the duration of mineralization bracketed by zircon dating of the successive tonalites at Batu Hijau, to have been completed within ~ 90 ky or less (Large et al., 2020). These considerations are consistent with our interpretation that the formation of retrograde paint veins have introduced the dominant fraction of metals at Batu Hijau.

Comparison with and implications for other porphyry Cu systems

Textural evidence for sulfide precipitation after quartz vein and veinlets similar to the paint veins noted in this study are widely reported from other porphyry systems. Although variations exists, similar veins are described as pale-green sericitic veins (Butte; Meyer, 1965; Rusk et al., 2008b), bornite-chalcopyrite-quartz-anhydrite veinlets with chlorite-sericite alteration halos (Los Pelambres; Sillitoe, 1973), discontinuous sulfide veinlets (Panguna; Eastoe, 1978), ore-bearing veins (Santa Rita; Reynolds and Beane, 1985), C-type veins (El Salvador; Gustafson and Quiroga, 1995; Batu Hijau; Arif and Baker, 2004), copper-gold veins (Grasberg; Pollard and Taylor, 2002), transitional to late chalcopyrite veins (Bajo de la Alumbrera; Proffett, 2003), type 2 chlorite veinlets (El Teniente; Cannell et al., 2005; Vry et al., 2010), sulfide-only veins (Bingham Canyon; Porter et al., 2012), or chalcopyrite hair-veinlets with chlorite selvages (Nuevo Chaquiro, Bartos et al., 2017). Based on sulfide-hosting vein types, two mineralization events are described for some deposits, including high-temperature sulfide precipitation during quartz vein formation followed by low-temperature sulfides along thin sulfide veinlets with chlorite alteration halos (e.g., Panguna, Eastoe, 1978; Nuevo Chaquiro, Bartos et al., 2017), whereby some paint veins crosscutting late-mineral intrusions were interpreted to indicate local metal remobilization (Proffett, 2003). For other deposits like Sierrita-Esperanza (Preece and Beane, 1982), Santa Rita

(Reynolds and Beane, 1985), Far Southeast (Hedenquist et al., 1998) and Escondida (Garza et al., 2001) most of the ore was interpreted to post-date high-temperature quartz vein formation associated with potassic alteration. Detailed fluid inclusion studies at Bingham Canyon (Landwing et al., 2010) and Grasberg (Mernagh et al., 2020) emphasize an alternative process of fluid expansion based on brine + vapor inclusions in quartz veins, arguing for gold + sulfide precipitation due to low-pressure metal de-complexation (cf. Migdisov et al., 2014). But even at Bingham Canyon (Landtwing et al., 2005, 2010), CL imaging of quartz stockwork veins shows a clear textural relationship between sulfides and a dull-luminescent quartz generation post-dating the main quartz veining event, similar to other porphyry systems (e.g., Rusk and Reed, 2002; Redmond et al., 2004; Klemm et al., 2007; Müller et al., 2010; Vry et al., 2010; Stefanova et al., 2014; Gregory, 2017).

A comparable mineralizing fluid to the one proposed here for Batu Hijau is reported from Far Southeast in the Philippines (Hedenquist et al., 1998) and El Teniente in Chile (Klemm et al., 2007). For Far Southeast, fluid inclusion and stable isotopic constraints indicated that a single-phase magmatic fluid separated into brine and vapor at paleo-depths below ~2 km (Shinohara and Hedenquist, 1997; Hedenquist et al., 1998). The early hypersaline liquid precipitated quartz veins followed by later sulfide precipitation from a low-salinity aqueous fluid during illite ± chlorite alteration (Hedenquist et al., 1998). These authors suggest sequential events of fluid injection with changing input compositions to explain the successive vein and alteration types. Similarly, for El Teniente, Klemm et al. (2007) proposed that quartz veins and sulfides have been formed from a common fluid but at different stages. Klemm et al. (2007) interpreted the Cu-Fe sulfides to be genetically linked to both, a vapor phase and its contracted single-phase low-salinity liquid derivative. For both deposits, the estimated temperature ranges of sulfide precipitation are comparable, 350°C in Far Southeast (Hedenquist et al., 1998) and 410° to 320°C in El Teniente (Klemm et al., 2007), and overlap with our results for Batu Hijau. However, the interpretation that quartz vein formation is temporally decoupled from sulfide precipitation on the scale of the hydrothermal system would imply that Cu contained in the early quartz-precipitating fluids is lost from the ore body and dispersed – in contrast to the dynamic spatial-temporal evolution of a single magmatic fluid proposed here for the retrograde stage at Batu Hijau.

At the Santa Rita deposit in New Mexico, Reynolds and Beane (1985) concluded that hypogene mineralization post-dates high-temperature quartz stockwork vein formation and associated potassic alteration and was formed from a low-salinity (< 9 wt.% $NaCl_{eq.}$) aqueous-like fluid at temperatures below 360°C. In contrast to Batu Hijau the mineralizing fluid was assumed to be dominantly of meteoric origin (Reynolds and Beane, 1985). Based on similar bulk chemical compositions of low salinity inclusions in early quartz and late pyrite veins, Rusk et al. (2008b) proposed that variable hydrothermal features are the result of changing fluid evolution paths of a single magma-derived fluid at Butte, Montana. Geochemical modelling of fluid-rock interactions demonstrated that a common magmatic fluid undergoing various cooling and depressurization paths could indeed be responsible for variable vein types and alteration mineral assemblages (Reed et al., 2013).

Many features of hypogene mineralization at Batu Hijau are common in descriptions of porphyry Cu systems worldwide, such as: the relative timing after the formation of quartz veins; the association with a dull-luminescent quartz generation and pale-green chlorite – white mica alteration along thin sulfide veinlets; and sulfide precipitation at moderate temperatures between 420° and 300°C. Consequently, the fluid evolution at Batu Hijau (Figs. 14 and 15) appears to be common for hypogene ore formation in porphyry systems, even though the physico-chemical mechanisms driving ore mineral precipitation are still debated and may vary between deposits (e.g., Williams-Jones and Heinrich, 2005; Kouzmanov and Pokrovski 2012; Migdisov et al. 2014; Henley and Seward, 2018). .

Conclusions

Hypogene ore minerals hosted within quartz stockwork veins at Batu Hijau comprise chalcopyrite, lesser bornite with minor amounts of digenite and gold in separate but co-precipitated grains. Textural relationships documented by CL imaging show that ore mineral precipitation, although spatially associated with quartz veins, temporally post-dates the main event of quartz deposition at any given point within the hydrothermal system and is related to superimposed paint veins associated with chlorite – white mica alteration. Thus, most, if not all, of the studied sulfides that macroscopically appear to be hosted by high-temperature quartz stockwork veins were introduced during the subsequent formation of paint veins.

Aqueous FIAs hosted within the mineralized quartz generation as well as chlorite and Ti-in-quartz thermometry suggest a narrow temperature window of sulfide precipitation between 360° and 310°C. The similar chemical composition of the high-temperature magmatic and the low-temperature mineralizing fluid implies that vein and alteration types are the result of progressively changing fluid evolution paths due to cooling and depressurization. Based on crosscutting relationships of different vein types, overprinting alteration mineral assemblages and the distribution of fluid inclusion types, we propose an evolution of the hydrothermal system at Batu Hijau that started with quartz vein formation in the high-temperature central parts (> 500°C) coeval with sub-economic sulfide precipitation in the low-temperature periphery (< 400°C). Inward-retreating isotherms led to telescoping of alteration styles, crosscutting of different vein types and most of the sulfide deposition after partial quartz dissolution within earlier quartz stockwork veins. Sulfides precipitated from a low-salinity single-phase aqueous fluid (~ 330°C, 1 to 8 wt.% $NaCl_{eq}$., 730 µg/g Cu on average) derived by re-homogenization of brine and vapor that were produced episodically by phase separation of the parental magmatic fluid on the preceding depressurization path, which thereby precipitated most of the locally predating vein quartz.

Although evidence for high-temperature sulfide precipitation has repeatedly been reported on the basis of macroscopic observations and might be of importance for Cu endowment in some porphyry systems, the CL observations from Batu Hijau — previously thought to be a dominantly high-temperature Cu-Au deposit — should be taken as a word of caution that macroscopic observations alone can be deceptive. Of the two endmember processes of Cu-Fe sulfide introduction and precipitation that contribute to porphyry Cu mineralization, the low-temperature process associated with inconspicuous chlorite – white mica-lined paint veins is commonly underestimated in our opinion. Phase separation of a single-phase hot magmatic fluid into dominant vapor and minor brine, followed by re-homogenization of these two fluids to an aqueous liquid of variably low salinity resembling the composition of the initial input fluid, could contribute to a temperature gap between the two endmember processes of Cu-Fe-sulfide precipitation.

Acknowledgments

We are grateful to PT. Amman Mineral Nusa Tenggara (previously PT. Newmont Nusa Tengarra) for access to the mine and logistic support during the three visits. In particular, we would like to thank Agung Naruputro and Eddy Priowasono for their help and advice during the sampling campaigns. Marcel Guillong and Christian Liebske are thanked for their help with the LA-ICP-MS analyses of fluid inclusions and the SEM element mapping, respectively. Furthermore, we would like to thank John M. Proffett for numerous thought-provoking discussions and suggestions during his visit at ETH in March 2020. Constructive reviews by Richard H. Sillitoe, Jeffrey W. Hedenquist, John M. Proffett and David R. Cooke helped to improve earlier versions of this manuscript. Financial support of this research project by ETH Zürich and the Swiss Science Foundation (Project 166151) is gratefully acknowledged.

References

Arif, J., and Baker, T., 2004, Gold paragenesis and chemistry at Batu Hijau, Indonesia: implications for gold-rich porphyry copper deposits: Mineralium Deposita, v. 39, p. 523-535.

Audétat, A., and Günther, D., 1999, Mobility and H_2O loss from fluid inclusions in natural quartz crystals: Contributions to Mineralogy and Petrology, v. 137, p. 1-14.

Audétat, A., Günther, D., and Heinrich, C.A., 1998, Formation of magmatic-hydrothermal ore deposit: Insights with LA-ICP-MS analysis of fluid inclusions: Science, v. 279, p. 2091-2094.

Barbieri, S., Bigioggero B., Boriani, A., Cattaneo, M., Cavallin, A., Eva C., Cioni, R., Gelmini, R., Giorgetti, F., Iaccarino, S., Innocenti, F., Marinelli, G., Slejko, D., and Sudradjat, A., 1987, The island of Sumbawa: a major structural discontinuity in the Indonesian Arc: Bollettino della Societa Geologica Italiana, v. 106, p. 547-620.

Bartos, P.J., Garcia, C., and Gil, J., 2017, The Nuevo Chaquiro Cu-Au-(Mo) porphyry deposit, Middle Cauca belt, Colombia: Geology, alteration, mineralization: Economic Geology, v. 112, p. 275-294.

Becker, S.P., Fall, A., and Bodnar, R.J., 2008, Synthetic fluid inclusions. XVII. PVTX properties of high salinity H_2O-NaCl solutions (>30 wt % NaCl): Application to fluid inclusions that homogenize by halite disappearance from porphyry copper and other hydrothermal ore deposits, Economic Geology, v. 103, p. 539-554.

Bodnar, R.J., 1995, Fluid-inclusion evidence for a magmatic source for metals in porphyry copper deposits: Mineralogical Association of Canada Short Course Series, v. 23, p. 139-152.

Bodnar, R.J., Burnham, C.W., and Sterner, S.M., 1985, Synthetic fluid inclusions in natural quartz. III. Determination of phase equilibrium properties in the system H_2O-NaCl to 1000°C and 1500 bars: Geochimica et Cosmochimica Acta, v. 49, p. 1861-1875.

944 Bourdelle, F., and Cathelineau, M., 2015, Low-temperature chlorite geothermometry: a graphical representation
945 based on a T - R^{2+} - Si diagam: European Journal of Mineralogy, v. 27, p. 617-626.

946 Bourdelle, F., Parra, T., Chopin, C., and Beyssac, O., 2013, A new chlorite geothermometer for diagenetic to low-grade
947 metamorphic conditions: Contributions to Mineralogy and Petrology, v. 165, p. 723-735.

948 Cannel, J., Cooke, D., Walshe, J., and Stein, H., 2005, Geology, mineralization, alteration, and structural evolution of
949 the El Teniente porphyry Cu-Mo deposit: Economic Geology, v. 100, p. 979-1003.

950 Cathelineau, M., 1988, Cation site occupancy in chlorites and illites as a function of temperature: Clay Minerals, v.
951 23, p. 471-485.

952 Cathles, L.M., 1981, Fluid flow and genesis of hydrothermal ore deposits: Economic Geology, v. 75, p. 424-457.

953 Chelle-Michou, C., Rottier, B., Caricchi, L., and Simpson, G., 2017, Tempo of magma degassing and the genesis of
954 porphyry copper deposits: Scientific Reports, v. 7, 40566.

955 Cline, J.S., and Bodnar, R.J., 1991, Can economic porphyry copper mineralization be generated by a typical calc-
956 alkaline melt: Journal of Geophysical Research-Solid Earth and Planets, v. 96, p. 8113-8126.

957 Clode, C., Proffett, J., Mitchell, P., and Munajat, I., 1999, Relationships of intrusion, wall-rock alteration and
958 mineralization in the Batu Hijau copper-gold porphyry deposit: in – Pacrim Congress, Bali, Indonesia, Proceedings,
959 Australasian Institute of Mining and Metallurgy, Publication Series No 4/99, p. 485-498.

960 Collins, P.L., 1979, Gas hydrates in CO_2-bearing fluid inclusions and the use of freezing data for estimation of salinity:
961 Economic Geology, v. 74, p. 1435-1444.

962 Crerar, D.A., and Barnes, H.L., 1976, Ore solution chemistry V. Solubilities of chalcopyrite and chalcocite assemblages
963 in hydrothermal solution at 200° to 350°C: Economic Geology, v. 71, p. 772-794.

964 Driesner, T., 2007, The system H_2O-NaCl. II. Correlations for molar volume, enthalpy, and isobaric heat capacity from
965 0 to 1000 degrees C, 1 to 5000 bar, and 0 to 1 X_{NaCl}. Geochimica et Cosmochimica Acta, v. 71, p. 4902-4919.

966 Driesner, T. and Heinrich, C.A., 2007, The system H_2O-NaCl. I. Correlation formulae for phase relations in
967 temperature-pressure-composition space from 0 to 1000°C, 0 to 5000 bar, and 0 to 1 X_{NaCl}. Geochimica et
968 Cosmochimica Acta, v. 71, p. 4880-4901.

969 Drummond, S.E., and Ohmoto, H., 1985, Chemical evolution and mineral deposition in boiling hydrothermal systems:
970 Economic Geology, v. 80, v. 126-147.

971 Eastoe C.J., 1978, A fluid inclusion study of the Panguna porphyry copper deposit, Bougainville, Papua New Guinea:
972 Economic Geology, v. 73, p. 721-748.

973 Fekete, S., Weis, P., Scott, S., and Driesner, T., 2018, Multiple stable isotope fronts during non-isothermal fluid flow:
974 Geochimica et Cosmochimica Acta, v. 223, p. 437-557.

975 Fiedrich, A.M., Laurent, O., Heinrich, C.A., and Bachmann, O., 2020, Melt and fluid evolution in an upper-crustal
976 magma reservoir, preserved by inclusions in juvenile clasts from the Kos Plateau Tuff, Aegean Arc, Greece:
977 Geochimica et Cosmochimica Acta, v. 280, p. 237-262.

978 Fiorentini, M.L., and Garwin, S.L., 2010, Evidence of mantle contribution in the genesis of magmatic rocks from the
979 Neogene Batu Hijau district in the Sunda Arc, South Western Sumbawa, Indonesia: Contributions to Mineralogy and
980 Petrology, v. 159, p. 819-837.

981 Fournier, R.O., 1967, The porphyry copper deposit exposed in the Liberty open-pit mine near Ely, Nevada. Part I.
982 Syngenetic formation: Economic Geology, v. 62, p. 57-81.

983 Fournier, R.O., 1983, A method of calculating quartz solubilities in aqueous sodium chloride solutions: Geochimica et
984 Cosmochimica Acta, v. 47, p. 579-586.

985 Fournier, R.O., 1999, Hydrothermal processes related to movement of fluid from plastic into brittle rock in the
986 magmatic-epithermal environment: Economic Geology, v. 94, p. 1193 – 1211.

987 Garwin, S.L., 2000, The setting, geometry and timing of intrusion-related hydrothermal systems in the vicinity of the
988 Batu Hijau porphyry copper-gold deposit, Sumbawa, Indonesia: unpublished PhD Thesis, Nedlands, Western
989 Australia, University of Western Australia, 320 p.

990 Garwin, S.L., 2002, The geological setting of intrusion-related hydrothermal systems near the Batu Hijau porphyry
991 copper-gold deposit, Sumbawa, Indonesia, Society of Economic Geologists Special Publication 9, p. 333-366.

992 Garza, R.A.P., Titley, S.R., and Pimentel, B.F., 2001, Geology of the Escondida porphyry copper deposit, Antofagasta
993 region, Chile: Economic Geology, v. 96, p. 307-324.

994 Gehrig, M., Lentz, H., and Franck, E.U., 1986, The system water – carbon dioxide – sodium chloride to 773 K and 300
995 MPa: Berichte der Bunsengesellschaft für physikalische Chemie, v. 90, p. 525-533.

996 Goldstein, R.H., and Reynolds, T.J., 1994, Systematics of fluid inclusions in diagenetic minerals: Society of Sedimentary
997 Geology Short Course, v. 31.

998 Gregory, M.J., 2017, A fluid inclusion and stable isotope study of the Pebble porphyry copper-gold-molybdenum
999 deposit, Alaska: Ore Geology Reviews, v. 80, p. 1279-1303.

1000 Guillong, M., Meyer, D.L., Allan, M.M., Heinrich, C.A., and Yardley, B.W.D., 2008a, SILLS: A Matlab-based program for
1001 the reduction of LA-ICP-MS data of homogeneous materials and inclusions: Mineralogical Association of Canada Short
1002 Course Series, v. 40, p. 328–333.

1003 Guillong, M., Latkoczy, C., Seo, J.H., Günther, D., and Heinrich, C.A., 2008b, Determination of sulfur in fluid inclusions
1004 by laser ablation ICP-MS: Journal of Analytical Atomic Spectrometry, v. 23, p. 1581-1589.

1005 Günther, D., Audétat, A., Frischknecht, R., and Heinrich, C.A., 1998, Quantitative analysis of major, minor and trace
1006 elements in fluid inclusions using laser ablation – inductively coupled plasma – mass spectrometry: Journal of
1007 Analytical Atomic Spectrometry, v. 13, p. 263-270.

1008 Gustafson, L.B., and Hunt, J.P., 1975, The porphyry copper deposit at El Salvador, Chile: Economic Geology, v. 70, p.
1009 857-912.

1010 Gustafson, L.B., and Quiroga, J., 1995, Patterns of mineralization and alteration below the porphyry copper orebody
1011 at El Salvador, Chile: Economic Geology, v. 90, p. 2-16.

1012 Hamilton, W., 1979, Tectonics of the Indonesian Region: U.S. Geological Survey, Professional Paper 1078, 345 pp.

1013 Harris, A.C., Kamenetsky, V.S., White, N.C., Achterbergh, E., and Ryan, C.G., 2003, Melt inclusions in veins: Linking
1014 magmas and porphyry Cu deposits: Science, v. 302, p. 2109-2111.

1015 Hedenquist, J.W., and Lowenstern, J.B., 1994, The role of magmas in the formation of hydrothermal ore deposits:
1016 Nature, v. 370, p. 519-527.

1017 Hedenquist, J.W., Arribas, A., Reynolds, T.J., 1998, Evolution of an intrusion-centered hydrothermal system: Far
1018 Southeast-Lepanto porphyry and epithermal Cu-Au deposits, Philippines: Economic Geology, v. 93, p. 373-404.

1019 Heinrich, C.A., Pettke, T., Halter, W.E., Aigner-Torres, M., Audétat, A., Günther, D., Hattendorf, B., Bleiner, D.,
1020 Guillong, M., and Horn, I., 2003, Quantitative multi-element analysis of minerals, fluid and melt inclusions by laser-
1021 ablation inductively-coupled-plasma mass-spectrometry: Geochimica et Cosmochimica Acta, v. 67, p. 3473-3497.

1022 Heithersay, P.S., and Walshe, J.L., 1995, Endeavour 26 North: A porphyry copper-gold deposit in the Late Ordovician,
1023 shoshonitic Goonumbla Volcanic Complex, New South Wales, Australia: Economic Geology, v. 90, p. 1506-1532.

1024 Henley, R.W., and McNabb, A., 1978, Magmatic vapor plumes and ground-water interaction in porphyry copper
1025 emplacement: Economic Geology, v. 73, p. 1-20.

1026 Henley, R.W., and Seward, T.M., 2018, Gas-solid reactions in arc volcanoes: ancient and modern: Reviews in
1027 Mineralogy and Geochemistry, v. 84, p. 309-349.

1028 Hey, M.H., 1954, A new review of chlorites: Mineralogical Magazine, v. 30, p. 277-292.

1029 Hezarkhani, A., 2009, Hydrothermal fluid geochemistry at the Chah-Firuzeh porphyry copper deposit, Iran: Evidence
1030 from fluid inclusions: Journal of Geochemical Exploration, v. 101, p. 254-264.

1031 Hezarkhani, A., Williams-Jones, A.E., and Gammons, C.H., 1999, Factors controlling copper solubility and chalcopyrite
1032 deposition in the Sungun copper deposit, Iran: Mineralium Deposita, v. 34, p. 770-783.

1033 Huang, R., and Audétat, A., 2012, The titanium-in-quartz (TitaniQ) thermobarometer: A critical examination and re-
1034 calibration: Geochimica et Cosmochimica Acta, v. 84, p. 75-89.

1035 Idrus, A., Kolb, J., and Meyer, F.M., 2009, Mineralogy, lithogeochemistry and elemental mass balance of the
1036 hydrothermal alteration associated with the gold-rich Batu Hijau porphyry copper deposit, Sumbawa Island,
1037 Indonesia: Resource Geology, v. 59, p. 215-230.

1038 Inoue, A., Meunier, A., Patrier-Mas, P., Rigault, C., Beaufort, D., and Vieillard, P., 2009, Application of chemical
1039 geothermometry to low-temperature trioctahedral chlorites: Clays and Clay Minerals, v. 57, p. 371-382.

1040 Inoue, A., Kurokawa, K., and Hatta, T., 2010, Application of chlorite geothermometry to hydrothermal alteration in
1041 Toyoha geothermal system, SW Hokkaido, Japan: Resource Geology, v. 60, p. 52-70.

1042 Jochum, K.P., Weis, U., Stoll, B., Kuzmin, D., Yang, Q., Raczek, I., Jacob, D.E., Stracke, A., Birbaum, K.,Frick,
1043 D.A., Günther, D. and Enzweiler, J., 2011, Determination of reference values for NIST SRM 610–617 glasses following
1044 ISO guidelines. Geostandards and Geoanalytical Research, v. 35, p. 397– 429.

1045 Jowett, E.C., 1991, Fitting iron and magnesium into the hydrothermal chlorite geothermometer: GAC/MAC/SEG Joint
1046 Annual Meeting, Toronto, May 27-29, 1991, Program with Abstracts 16.

1047 Kesler, S.E., Chryssoulis, S.L., and Simon, G., 2002, Gold in porphyry copper deposits: its abundance and fate: Ore
1048 Geology Reviews, v. 21, p. 103-124.

1049 Klemm, L.M., Pettke, T., and Heinrich, C.A., 2007, Hydrothermal evolution of the El Teniente deposit, Chile: Porphyry
1050 Cu-Mo ore deposition from low-salinity magmatic fluids: Economic Geology, v. 102, p. 1021-1045.

1051 Kouzmanov, K., and Pokrovski, G.S., 2012, Hydrothermal controls on metal distribution in porphyry Cu (-Mo-Au)
1052 systems: Society of Economic Geologists Special Publication 16, p. 573-618.

1053 Lambrecht G., and Diamond L.W., 2014, Morphological ripening of fluid inclusions and coupled zone-refining in quartz
1054 crystals revealed by cathodoluminescence imaging: Implications for CL-petrography, fluid inclusion analysis and trace
1055 element geothermometry: Geochimica et Cosmochimica Acta, v. 141, p. 381-406.

1056 Lamy-Chappuis, B., Heinrich, C.A., Driesner, T., and Weis, P., 2020, Mechanisms and patterns of magmatic fluid
1057 transport in cooling hydrous intrusions: Eart and Planetary Science Letters, v. 535, 116111.

1058 Landtwing, M.R., and Pettke, T., 2005, Relationships between SEM-cathodoluminescence response and trace-
1059 element composition of hydrothermal quartz, American Mineralogist, v. 90, p. 122-131.

1060 Landtwing, M.R., Pettke, T., Werner, H.E., Heinrich, C.A., Redmond, P.B., Einaudi, M.T., and Kunze K., 2005, Copper
1061 deposition during quartz dissolution by cooling magmatic-hydrothermal fluids: The Bingham porphyry: Earth and
1062 Planetary Science Letters, v. 235, p. 229-243.

1063 Landtwing, M.R., Furrer, C., Redmond, P.B., Pettke, T., Guillong, M., and Heinrich, C.A., 2010, The Bingham Canyon
1064 porphyry Cu-Mo-Au deposit. III. Zoned copper-gold ore deposition by magmatic vapor expansion: Economic Geology,
1065 v. 105, p. 91-118.

1066 Large, S.J.E., Wotzlaw, J.F., Guillong, M., von Quadt, A., and Heinrich, C.A., 2020, Resolving the timescales of magmatic
1067 and hydrothermal processes associated with porphyry deposit formation using zircon U-Pb petrochronology:
1068 Geochronology, v. 2, p. 209-230.

1069 Lecumberri-Sanchez, P, Steele-MacInnis, M., and Bodnar, R.J., 2012, A numerical model to estimate trapping
1070 conditions of fluid inclusions that homogenize by halite disappearance: Geochimica et Cosmochimica Acta, v. 92, p.
1071 14-22.

1072 Lerchbaumer, L., and Audétat, A., 2012, High Cu concentrations in vapor-type fluid inclusions: An artifact?:
1073 Geochimica et Cosmochimica Acta, v. 88, p. 255-274.

1074 Liebscher, A., and Heinrich, C.A., 2007, Fluid-fluid interactions in the Earth's lithosphere: Reviews in Mineralogy and
1075 Geochemistry, v. 65, p. 1-13.

1076 Liebske, C., 2015, iSpectra: An open source toolbox for the analysis of spectral images recorded on scanning electron
1077 microscopes: Microscopy and Microanalysis, v. 21, p. 1006-1016.

1078 Liu, W., and McPhail, D.C., 2005, Thermodynamic properties of copper chloride complexes and copper transport in
1079 magmatic-hydrothermal solutions: Chemical Geology, v. 221, p. 21-39.

1080 Lowell, J.D., 1974, Regional characteristics of porphyry copper deposits of the Southwest: Economic Geology, v. 69,
1081 p. 601-617.

1082 Lowell J.D., and Guilbert, J.M., 1970, Lateral and vertical alteration-mineralization zoning in porphyry ore deposits:
1083 Economic Geology, v. 65, p. 373-408.

1084 Maryono, A., Harrison, R.L., Cooke, D.R., Rompo, I., and Hoschke, T.G., 2018, Tectonics and geology of porphyry Cu-
1085 Au deposits along the Eastern Sunda Magmatic Arc, Indonesia: Economic Geology, v. 113, p. 7-38.

1086 McDowell, S.D., and Elders, W.A., 1980, Authigenic layer silicate minerals in borehole Elmore 1, Salton Sea
1087 geothermal field, California, USA: Contributions to Mineralogy and Petrology, v. 74, p. 293-310.

1088 McInnes, B.I.A., Evans, N.J., Fu, F.Q., Garwin, S., Belousova, E., Griffin, W.L., Bertens, A., Sukarna, D., Permanadewi,
1089 S., Andrew, R.L., and Deckart, K., 2005, Thermal history analysis of selected, Chilean, Indonesian, and Iranian porphyry
1090 Cu-Mo-Au deposits, *in* Porter T.M., ed., Super porphyry copper and gold deposits: A global perspective: Porter
1091 Geoconsultancy Publishing, de Adelaide, Australia, p. 27-42.

1092 Meldrum, S.J., Aquino, R.S., Gonzales, R.I., Burke, R.J., Suyadi, A., Irianto, B., Clarke, D.S., 1994, The Batu Hijau
1093 porphyry copper-gold deposit, Sumbawa Island, Indonesia: Journal of Geochemical Exploration, v. 50, p. 203-220.

1094 Mernagh, T.P., Leys, C., and Henley, R.W., 2020, Fluid inclusion systematics in porphyry copper deposits: The super-
1095 giant Grasberg deposit, Indonesia, as a case study: Ore Geology Reviews, v. 123, 103570.

1096 Meyer, C., 1965, An early potassic type of wall-rock alteration at Butte, Montana: American Mineralogist, v. 50, p.
1097 1717-1722.

1098 Migdisov, A.A., Bychkov, A.Y., Williams-Jones, A.E., and van Hinsberg, V.J., 2014, A predictive model for the transport
1099 of copper by HCl-bearing water vapor in ore-forming magmatic-hydrothermal systems: Implications for copper
1100 porphyry ore formation: Geochimica et Cosmochimica Acta, v. 129, p. 33-53.

1101 Monecke, T., Monecke, J., Reynolds, T.J., Tsuruoka, S., Bennett, M.M., Skewes, W.B., and Palin, R.M., 2018, Quartz
1102 solubility in the H_2O-NaCl system: A framework for understanding vein formation in porphyry copper deposits:
1103 Economic Geology, v. 113, p. 1007-1046.

1104 Müller, A., Herrington, R., Armstrong, R., Seltmann, R., Kirwin, D.J., Stenina, N.G., and Kronz, A., 2010, Trace elements
1105 and cathodoluminescence of quartz in stockwork veins of Mongolian porphyry-style deposits: Mineralium Deposita,
1106 v. 45, p. 707-727.

1107 Murakami, H., Seo, J.M., and Heinrich, C.A., 2010, The relation between Cu/Au ratio and formation depth of porphyry-
1108 style Cu – Au ± Mo deposits: Mineralium Deposita, v. 45, p. 11-21.

1109 Nash, T.J., 1976, Fluid-inclusion petrology – data from porphyry copper deposits and applications to exploration: U.S.
1110 Geological Survey Professional Paper 907-D, v. 907, p. 1-16.

1111 Pettke, T., Oberli, F., Audétat, A., Guillong, M., Simon, A.C., Hanley, J.J., and Klemm, L.M., 2012, Recent developments
1112 in element concentration and isotope ratio analysis of individual fluid inclusions by laser ablation single and multiple
1113 collector ICP-MS: Ore Geology Reviews, v. 44, p.10-38.

1114 Pokrovski, G.S., Roux, J., and Harrichoury, J.C., 2005, Fluid density control on vapor-liquid partitioning of metals in
1115 hydrothermal systems: Geology, v. 33, p. 657-660.

1116 Pollard, P.J., and Taylor, 2002, Paragenesis of the Grasberg Cu-Au deposit, Irian Jaya, Indonesia: results from logging
1117 section 13: Mineralium Deposita, v. 37, p. 117-136.

1118 Porter, J.P, Schroeder, K., and Austin, G., 2012, Geology of the Bingham Canyon Cu-Mo-Au deposit, Utah: Society of
1119 Economic Geologists Special Publication 16, p. 127-146.

1120 Preece, R.K., and Beane, R.E., 1982, Contrasting evolutions of hydrothermal alteration in quartz monzonite and quartz
1121 diorite wall rocks at the Sierrita porphyry copper deposit, Arizona: Economic Geology, v. 77, p. 1621-1641.

1122 Proffett, J.M., 2003, Geology of the Bajo de la Alumbrera porphyry copper-gold deposit, Argentina: Economic
1123 Geology, v. 98, p. 1535-1574.

1124 Proffett, J.M., 2009, High Cu grades in porphyry Cu deposits and their relationship to emplacement depth of
1125 magmatic sources: Geology, v. 37, p. 675-678.

1126 Redmond, P.B., Einaudi, M.T., Inan, E.E., Landtwing, M.R., Heinrich, C.A., 2004, Copper ore formation by fluid cooling
1127 in porphyry copper deposits: new insights from cathodoluminescence petrography combined with fluid inclusion
1128 microthermometry: Geology, v. 32, p. 217-220.

1129 Redmond, P.B., and Einaudi, M.T., 2010, The Bingham Canyon porphyry Cu-Mo-Au deposit. I. Sequence of intrusions,
1130 vein formation, and sulfide deposition: Economic Geology, v. 105, p. 43-68.

1131 Reed, M., Rusk, B., and Palandri, J., 2013, The Butte magmatic-hydrothermal system: One fluid yields all alteration
1132 and veins: Economic Geology, v. 108, p. 1379-1396.

1133 Reynolds, T.J., and Beane, R.E., 1985, Evolution of hydrothermal fluid characteristics at the Santa Rita, New Mexico,
1134 porphyry copper deposit: Economic Geology, v. 80, p. 1328-1347.

1135 Roedder, E., 1971, Fluid inclusion studies on the porphyry-type ore deposits at Bingham, Utah, Butte, Montana, and
1136 Climax, Colorado: Economic Geology, v. 66, p. 98-118.

1137 Roedder, E., 1984, Fluid inclusions: Reviews in Mineralogy, v. 12, p. 71-77.

1138 Roedder, E., and Bodnar, R.J., 1980, Geological pressure determinations from fluid inclusion studies, Annual Review
1139 of Earth and Planetary Sciences, v. 8, 263-301.

1140 Rosso, K.A., and Bodnar, R.J., 1995, Microthermometric and Raman spectroscopic detection limits of CO_2 in fluid
1141 inclusions and the Raman spectroscopic characterization of CO_2: Geochimica et Cosmochimica Acta, v. 59, p. 3961-
1142 3975.

1143 Rusk, B.G., and Reed, M.H., 2002, Scanning electron microscope-cathodoluminescence analysis of quartz reveals
1144 complex growth histories in veins from the Butte porphyry copper deposit, Montana: Geology, v. 30, p. 727-730.

1145 Rusk, B.G., Lowers, H.A., and Reed, M.H., 2008a, Trace elements in hydrothermal quartz: Relationships to
1146 cathodoluminescence textures and insights into vein formation: Economic Geology, v. 36, p. 547-550.

1147 Rusk, B.G., Reed, M.H., and Dilles, J.H., 2008b, Fluid inclusion evidence for magmatic-hydrothermal fluid evolution in
1148 the porphyry copper-molybdenum deposit at Butte, Montana: Economic Geology, v. 103, p. 307-334.

1149 Ryan, C.G., McInnes, B.I.A., Williams, P.J., Dong, G., Win, T.T., and Yeats, C.J., 2001, Imaging fluid inclusion content
1150 using the new CSIRO-GEMOC nuclear microprobe: Nuclear Instruments and Methods In Physical Research, v. 181, p.
1151 570 – 577.

1152 Schlöglová, K., 2018, Fluid inclusion analysis of other host minerals besides quartz: published PhD Thesis, Zürich,
1153 Switzerland, ETH Zürich, 250 p.

1154 Schlöglová, K., Wälle, M., and Heinrich, C.A., 2017, LA-ICP-MS analysis of fluid inclusions: contamination effects
1155 challenging micro-analysis of elements close to their detection limit: Journal of analytical atomic spectrometry, v. 32,
1156 p. 1052-1063.

1157 Seedorff, E., Dilles, J.H., Proffett, J.M., Einaudi, M.T., Zurcher, L., Stavast, W.J.A., Johnson, D.A., and Barton, M.D.,
1158 2005, Porphyry deposits: Characteristics and origin of hypogene features: Economic Geology, v. 100, p. 251-298.

1159 Seo, J.H., Guillong, M., and Heinrich, C.A., 2009, The role of sulfur in the formation of magmatic-hydrothermal copper-
1160 gold deposits: Earth and Planetary Science Letters, v. 282, p. 323-328.

1161 Seo, J.H., Guillong, M., Aerts, M., Zajacz, Z., and Heinrich, C.A., 2011, Microanalysis of S, Cl, and Br in fluid inclusion
1162 by LA-ICP-MS: Chemical Geology, v. 284, p. 35-44.

1163 Seo, J.H., and Heinrich, C.A., 2013, Selective copper diffusion into quartz-hosted vapor inclusions: Evidence from
1164 other host minerals, driving forces, and consequences for Cu-Au ore formation: Geochimica et Cosmochimica Acta,
1165 v. 113, p. 60-69.

1166 Setyandhaka, D., Arif, J., and Proffett, J.M., 2008, Characteristics of the root of a classic Cu-Au porphyry system: The
1167 Batu Hijau porphyry deposit, Indonesia: PACRIM Congress 2008, Australasian Institute of Mining and Metallurgy
1168 (AusIMM), Brisbane, Australia, November 24–26, 2008, Proceedings, 15 p.

1169 Shinohara, H., and Hedenquist, J.W., 1997, Constraints on magma degassing beneath the Far Southeast porphyry Cu-
1170 Au deposit, Philippines: Journal of Petrology, v. 38, p. 1741-1752.

1171 Sillitoe, R.H., 1973, Geology of the Los Pelambres porphyry copper deposit, Chile: Economic Geology, v. 68, p. 1-10.

1172 Sillitoe, R.H., 1979, Some thoughts on gold-rich porphyry copper deposits: Mineralium Deposita, v. 14, p. 161-174.

1173 Sillitoe, R.H., 1994, Erosion and collapse of volcanoes: Causes of telescoping in intrusion-centered ore deposits:
1174 Geology, v. 22, p. 945-948.

1175 Sillitoe, R.H., 1997, Characteristics and controls of the largest porphyry copper-gold and epithermal gold deposits in
1176 the circum-Pacific region: Australian Journal of Earth Sciences, v. 44, p. 373-388.

1177 Sillitoe, R.H., 2010, Porphyry copper systems: Economic Geology, v. 105, p. 3-41.

1178 Simon, G., Kesler, S.E., Essene, E.J., and Chryssoulis, S.L., 2000, Gold in porphyry copper deposits: Experimental
1179 determination of the distribution of gold in the Cu-Fe-S system at 400 to 700°C: Economic Geology, v. 95, p. 259-270.

1180 Steele-MacInnis, M., Lecumberri-Sanchez, P., and Bodnar, R.J., 2012, HokieFlincs_H_2O-NaCl: A Microsoft excel
1181 spreadsheet for interpreting microthermometric data from fluid inclusions based on the PVTX properties of H_2O-
1182 NaCl: Computers and Geosciences, v. 49, p. 334-337.

1183 Steele-MacInnis, M., Ridley, J., Lecumberri-Sanchez, P., Schlegel, T.U., and Heinrich, C.A., 2016, Application of low-
1184 temperature microthermometric data for interpreting multicomponent fluid Inclusion compositions: Earth-Science
1185 Reviews, v. 159, p. 14-35.

1186 Stefanova, E., Driesner, T., Zajacz, Z., Heinrich, C.A., Petrov, P., and Vasilev, Z., 2014, Melt and fluid inclusions in
1187 hydrothermal veins: The magmatic to hydrothermal evolution of the Elatsite porphyry Cu-Au deposit, Bulgaria:
1188 Economic Geology, v. 109, p. 1359-1381.

1189 Sterner, S.M., 1992, Homogenization of fluid inclusions to the vapor phase; the apparent homogenization
1190 phenomenon: Economic Geology, v. 87, p. 1616-1623.

1191 Ulrich, T., Günther, D., and Heinrich, C.A., 2002, The evolution of a porphyry Cu-Au deposit, based on LA-ICP-MS
1192 analysis of fluid inclusions: Bajo de la Alumbrera, Argentina: Economic Geology, v. 97, p. 1889-1920.

Vry, V.H., Wilkinson, J.J., Seguel, J., Millán, J., 2010, Multistage intrusion, brecciation, and veining at El Teniente, Chile: Evolution of a nested porphyry system: Economic Geology, v. 105, p. 119-153.

Walshe, J.L., 1986, A six-component chlorite solid solution model and the conditions of chlorite formation in hydrothermal and geothermal systems: Economic Geology, v. 81, p. 681-703.

Wark, D.A., and Watson, E.B., 2006, TitaniQ: a titanium-in-quartz geothermometer: Contributions to Mineralogy and Petrology, v. 152, p. 743-754.

Weis, P., 2015, The dynamic interplay between saline fluid flow and rock permeability in magmatic-hydrothermal systems: Geofluids, v. 15, p. 350-371.

Weis, P., Driesner, T., and Christoph, C.A., 2012, Porphyry-copper ore shells form at stable pressure-temperature fronts within dynamic fluid plumes: Science, v. 338, p. 1613-1616.

Weiland, R.J., and Cloos, M., 1996, Pliocene-Pleistocene asymmetric unroofing of the Irian fold belt, Irian Jaya, Indonesia: Apatite fission-track thermochronology: Geological Society of America Bulletin, v. 108, p. 1438-1449.

Wilkinson, J.J., Chang, Z., Cooke, D.R., Baker, M.J., Wilkinson, C.C., Inglis, S., Chen, H., and Gemmell, J.B., 2015, The chlorite proximitor: A new tool for detecting porphyry ore deposits: Journal of Geochemical Exploration, v. 152, p. 10-26.

Williams-Jones, A.E., and Heinrich, C.A., 2005, Vapor transport of metals and the formation of magmatic-hydrothermal ore deposits: Economic Geology, v. 100, p. 1287-1312.

Zajacz, Z., Hanley, J.J., Heinrich, C.A., Halter, W.E., Guillong, M., 2009, Diffusive reequilibration of quartz-hosted silicate melt and fluid inclusions: Are all metal concentrations unmodified?: Geochimica et Cosmochimica Acta, v. 73, p. 3013-3027.

Zajacz, Z., Candela, P.A., and Piccoli, P.M., 2017, The partitioning of Cu, Au and Mo between liquid and vapor at magmatic temperatures and its implications for the genesis of magmatic-hydrothermal ore deposits: Geochimica et Cosmochimica Acta, v. 207, p. 81-101.

Zwyer, T., 2010, Temporal and spatial evolution of hydrothermal, ore-related fluids in the Batu Hijau porphyry copper-gold deposit, Sumbawa (Indonesia): unpublished Master Thesis, Zürich, Switzerland, Eidgenössische Technische Hochschule (ETH), 54 p.

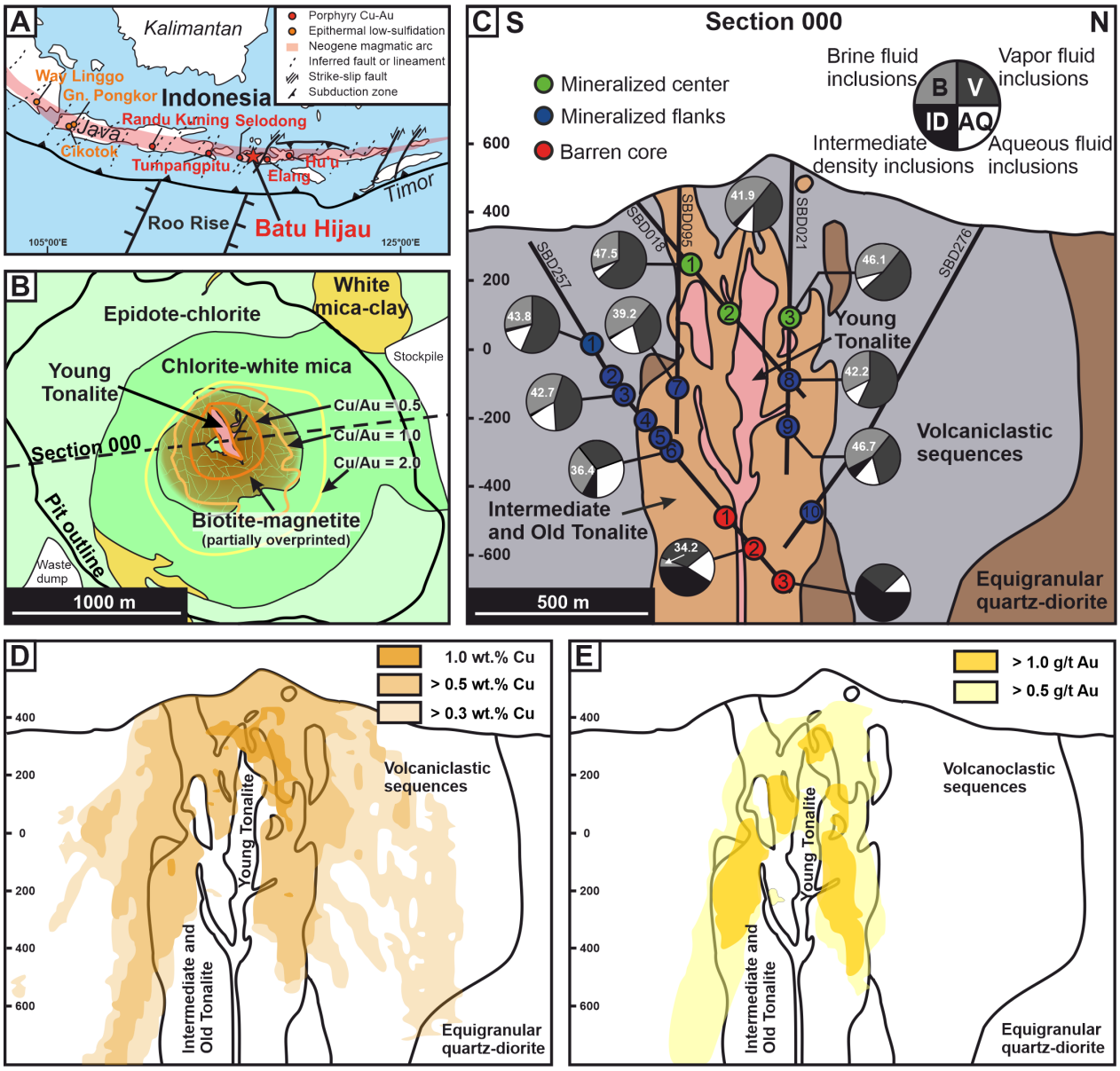

Figure 1: A) Location of Batu Hijau mine as well as other porphyry and epithermal deposits within the Neogene Sunda-Banda arc system, Indonesia (modified from Garwin, 2000). B) Alteration pattern of Batu Hijau at mine-scale with outline of Cu/Au ratios increasing from the center to the periphery (based on internal company reports provided by PT Amman Mineral Internasional). C) Sample locations along drill holes on cross-section 000 and distribution of fluid inclusion types. Sample numbers refer to samples listed in Table 1. Average bulk salinities ($NaCl_{eq.}$) for brine fluid inclusions are listed as small numbers in white in the respective parts of the pie charts. D) Cu ore-grades, and E) Au ore grades along the same cross-section (provided by PT Amman Mineral Internasional).

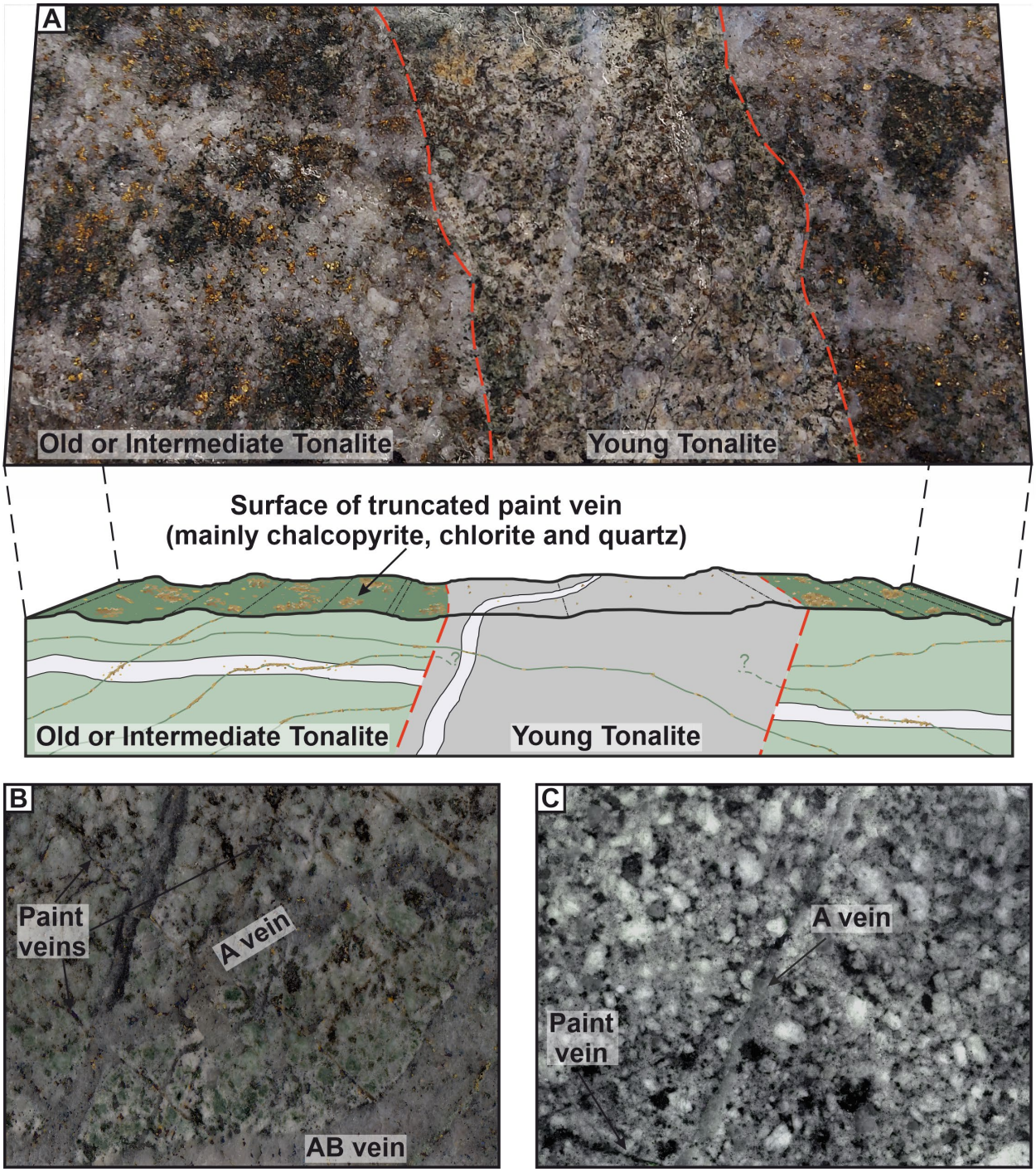

Figure 2: Intersection relations and petrographic differences between low-grade Young Tonalite (YT) and economically mineralized rocks (OT and IT) at Batu Hijau. A) Surface of paint vein in OT or IT truncated by YT. Although unambiguous truncations of paint veins at the contact to the YT are uncommon, the significantly lower amount of chalcopyrite and chlorite in YT compared to the older OT or IT indicates that the paint vein was truncated by the YT. B) and C) The general abundance of paint veins in and color of economically and sub-economically mineralized samples is another indication that paint veins and low-temperature mineralization largely pre-date the YT: in the OT/IT (B, sample SBD 18 419m) paint veins are abundant and chlorite – white mica alteration is intensive resulting in the characteristic green color of highly mineralized rocks, whereas in the YT (C) paint veins are less common resulting in a less intense chlorite – white mica overprint so that the grey-white color of the porphyritic rock is largely preserved.

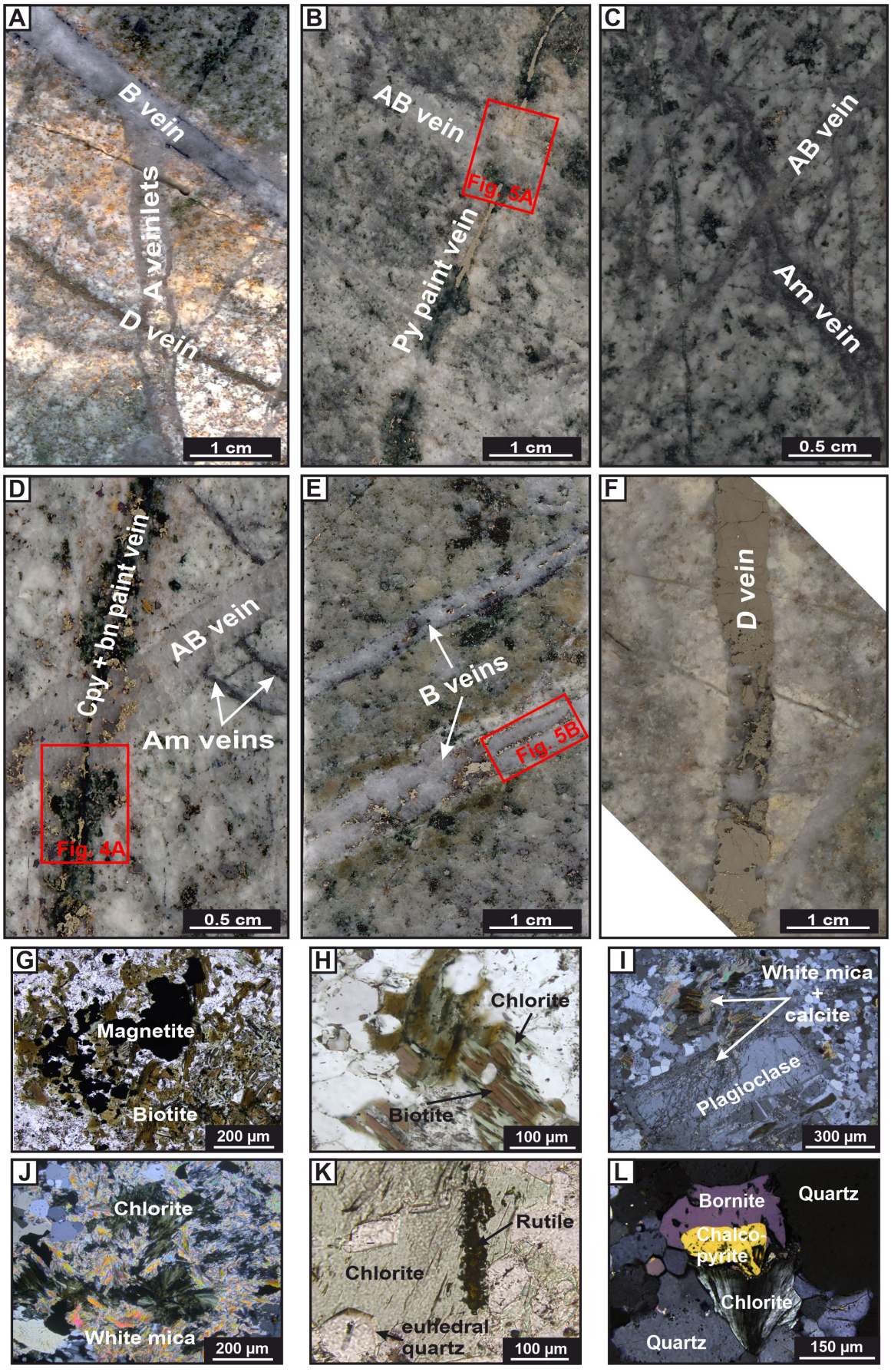
A
B vein
D vein
A veinlets
1 cm
B
AB vein
Fig. 5A
Py paint vein
1 cm
C
AB vein
Am vein
0.5 cm
D
Cpy + bn paint vein
AB vein
Am veins
Fig. 4A
0.5 cm
E
B veins
Fig. 5B
1 cm
F
D vein
1 cm
G
Magnetite
Biotite
200 µm
H
Chlorite
Biotite
100 µm
I
White mica
+
calcite
Plagioclase
300 µm
J
Chlorite
White mica
200 µm
K
Rutile
Chlorite
euhedral
quartz
100 µm
L
Bornite
Quartz
Chalco-
pyrite
Chlorite
Quartz
150 µm

1240

Figure 3: Examples of vein types and associated alteration assemblages from Batu Hijau. A) A-veins crosscut by molybdenite-bearing B-vein and D-vein associated with feldspar-destructive alteration from the barren core (SBD 257 1226m). B) pyrite-dominated paint-vein with characteristic chlorite-white mica alteration below the ore-shell apparently crosscut by barren AB-veins (SBD 257 1132m). C) Typical magnetite-rich quartz stockwork veins in the barren core crosscut by AB-vein (SBD 257 925m). D) Chalcopyrite (cpy) and bornite (bn)-rich paint vein with characteristic chlorite-white mica alteration halo crosscutting AB-vein within the highly mineralized part of Batu Hijau (SBD 18 416m). E) Two parallel B-veins with sulfide centerline (SBD 18 230m). F) Thick pyrite-dominated D-vein with quartz associated with feldspar-destructive white mica-clay alteration (SBD 276 1002m). G) Transmitted light image of K-silicate alteration in the barren core with shreddy biotite and opaque magnetite replacing mafic phenocryst (SBD 257 1132m). H) Partial alteration of presumably primary biotite to chlorite (SBD 257 507m). I) Polarized transmitted light image of euhedral biotite and Ca-rich plagioclase with Na-rich rim replaced by white mica and calcite along fractures (SBD 18 416m). J) Chlorite rosettes with white mica along paint-vein containing chalcopyrite and bornite in the high-grade ore zone under polarized transmitted light (SBD 18 416m). K) Transmitted light image of brown, blocky rutile within secondary chlorite as result of biotite replacement (SBD 18 416m). L) Combined reflected and polarized transmitted light image of bornite and chalcopyrite associated with chlorite rosette within B-vein in the high-grade ore zone (SBD 95 601m).

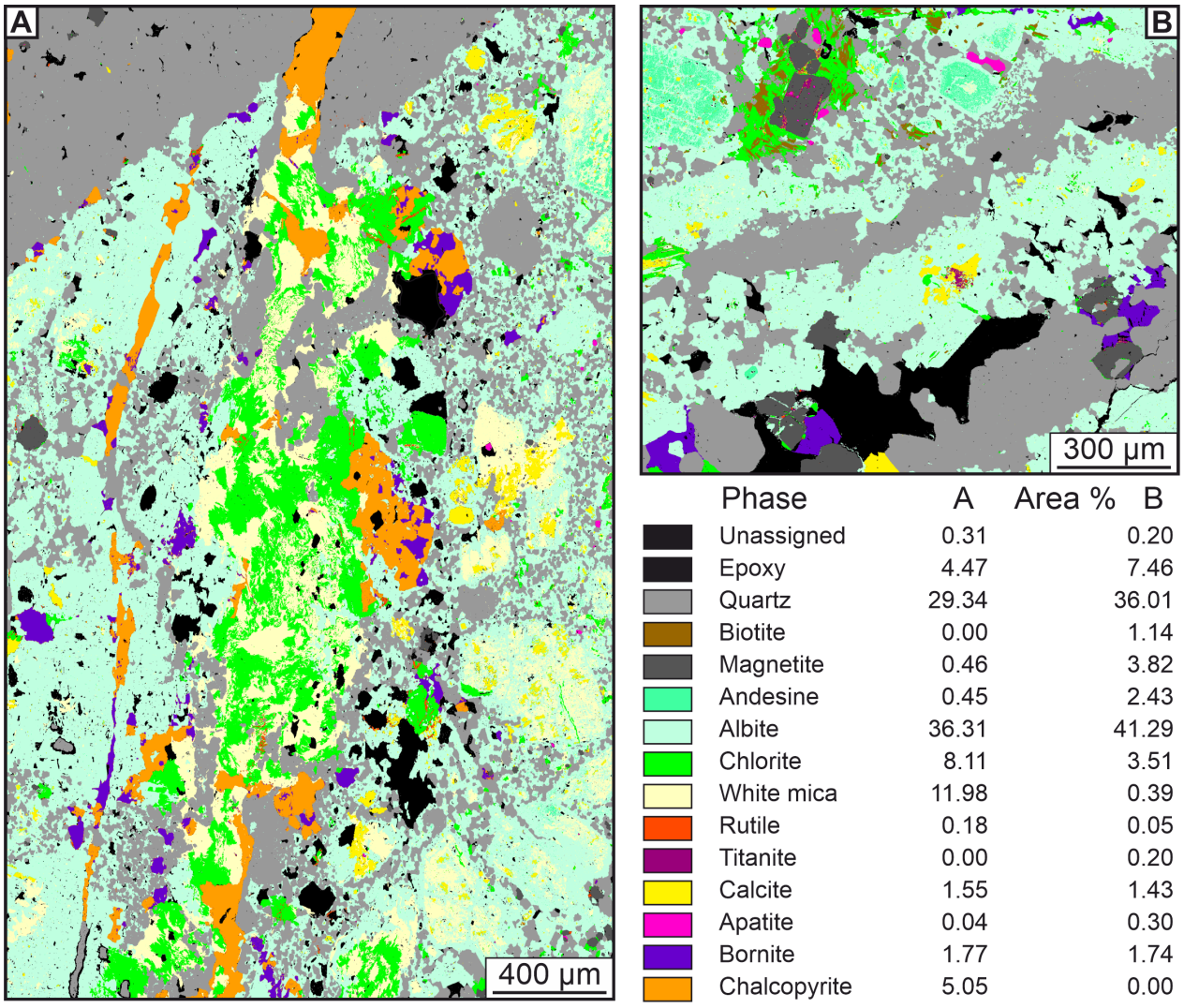

Figure 4: Phase maps generated with iSpectra (Liebske, 2015) of paint veins with associated alteration. A) Paint vein containing chalcopyrite and bornite with distinctive chlorite-white mica alteration halo, crosscutting an AB vein as shown in Figure 3D (SBD 18 416m). B) Bornite-dominated paint vein associated with incipient chlorite-white mica alteration (more andesine, magnetite and biotite is still present; SBD 21 797). Note the increased porosity along and within these paint veins, now filled with epoxy.

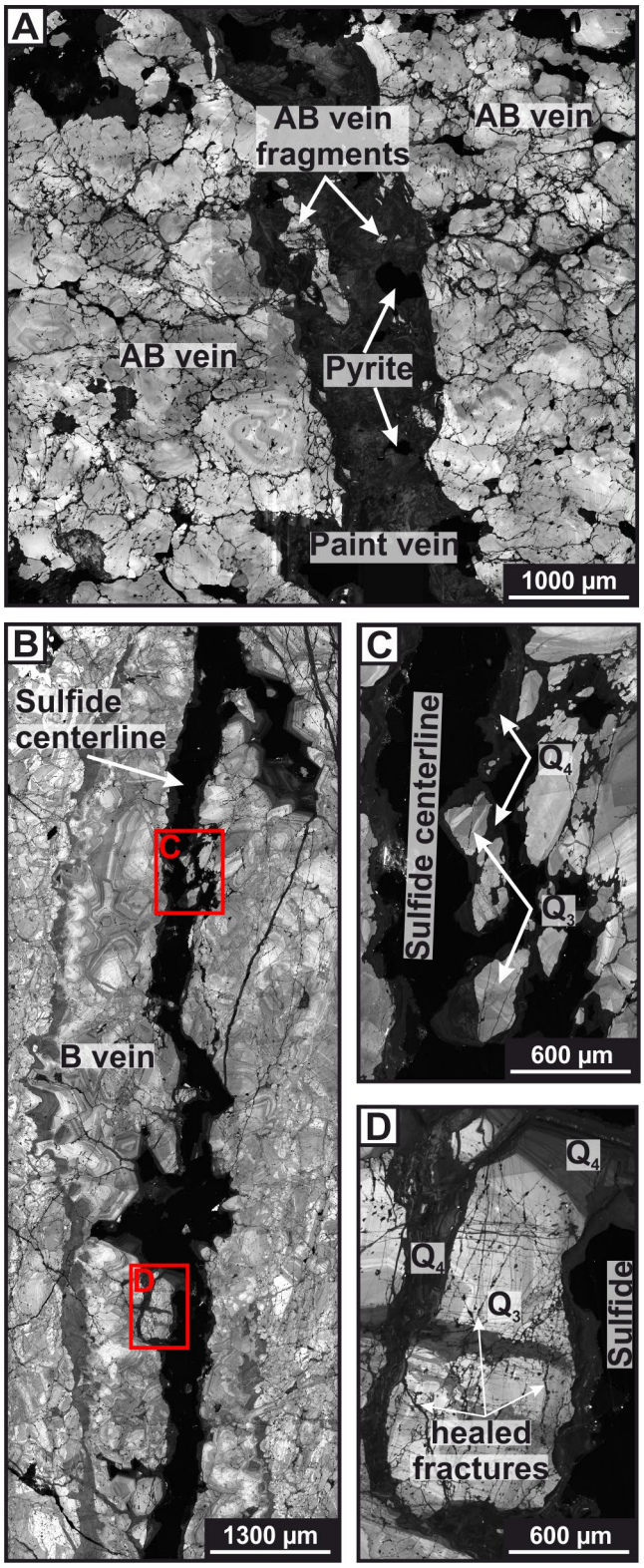

Figure 5: Cathodoluminescence images revealing textures of different hydrothermal quartz generations. A) Pyrite-bearing paint vein crosscutting AB vein. Such crosscutting relationships are difficult to interpret by eye or transmitted light observations, as in Figure 2B. Fragments of earlier vein generations can also obscure fluid inclusion distribution along such veins because buried fragments containing fluid inclusions associated with earlier quartz generations are not visible by CL imaging of the surface (SBD 257 1132m). B) B vein with large euhedral Q_3 grains and sulfide centerline as shown in Figure 2E (SBD 18 230m). Note that many different quartz generations are visible progressively overgrowing earlier quartz from the rim to the center. C) Enlarged section

of sulfide centerline showing Q_4 sheathing the sulfides. The wavy contact between Q_3 and Q_4 indicates an interval of quartz dissolution before renewed precipitation of quartz. D) Enlarged section of Q_3 grains coated by Q_4 associated with sulfide centerline. Note that the micro-fracture network produced by trails of fluid inclusions leaching trace elements from the hosting quartz (Lambrecht and Diamond, 2014) are truncated by Q_4. This is clear evidence for the pseudosecondary origin of the fluid inclusions hosted by Q_3 relative to Q_4.

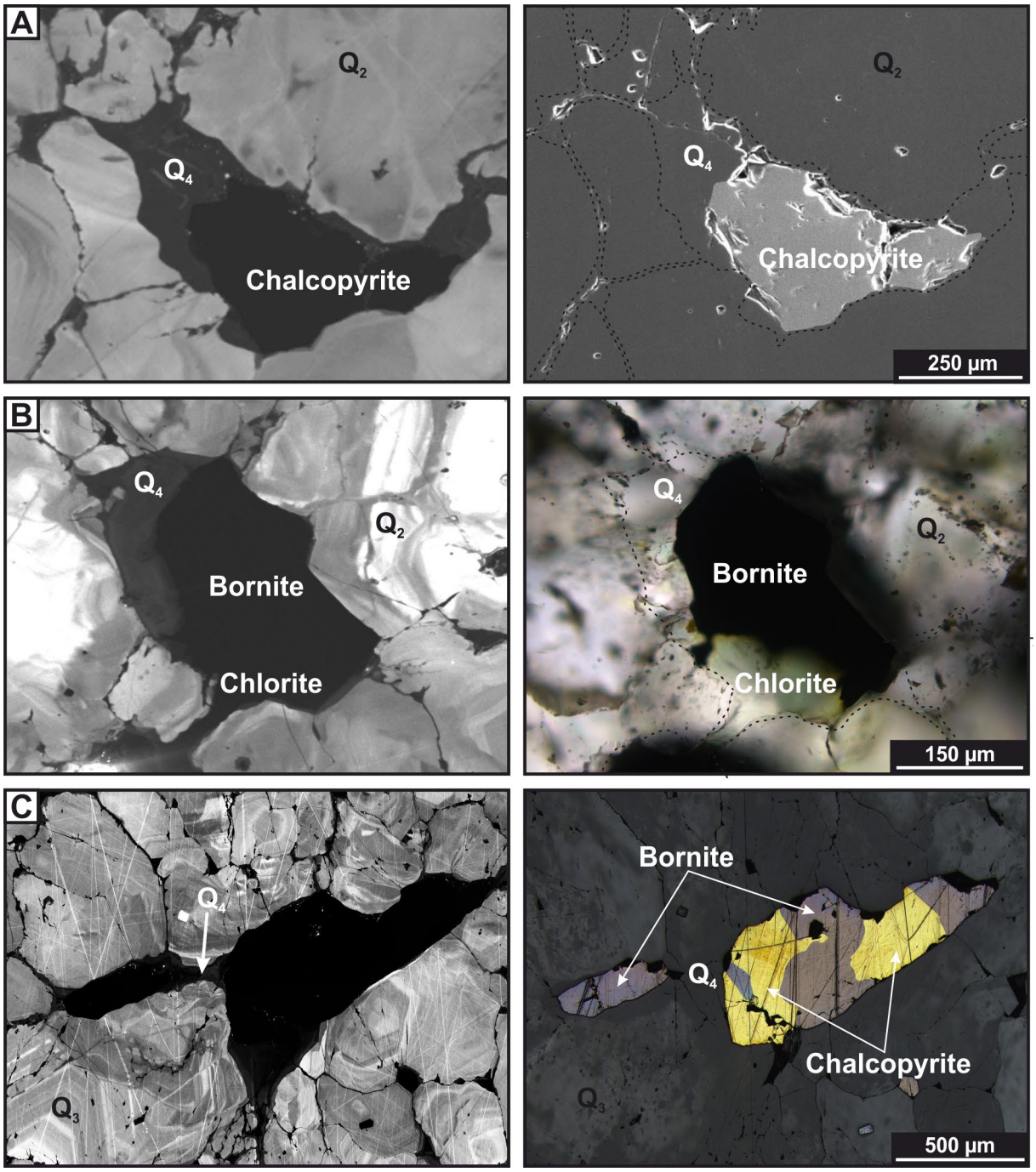

Figure 6: Textural context of sulfides hosted by hydrothermal quartz veins. A) CL image (left) and back-scattered electron image (right) of chalcopyrite grain hosted in AB vein. The sulfide grain is completely coated by Q_4 associated with paint veins as explained in the text (SBD 257 637m). B) CL imagine (left) and transmitted light image (right) of bornite grain associated with radial growing chlorite rosette. Both minerals are coated by Q_4 (SBD 21 797m). C) CL image (left) and reflected light image (right) of bornite and chalcopyrite along discontinuous sulfide centerline of B vein. Sulfide grains are connected by Q_4-filled cracks crosscutting euhedral Q_3 grains (SBD 18 416m).

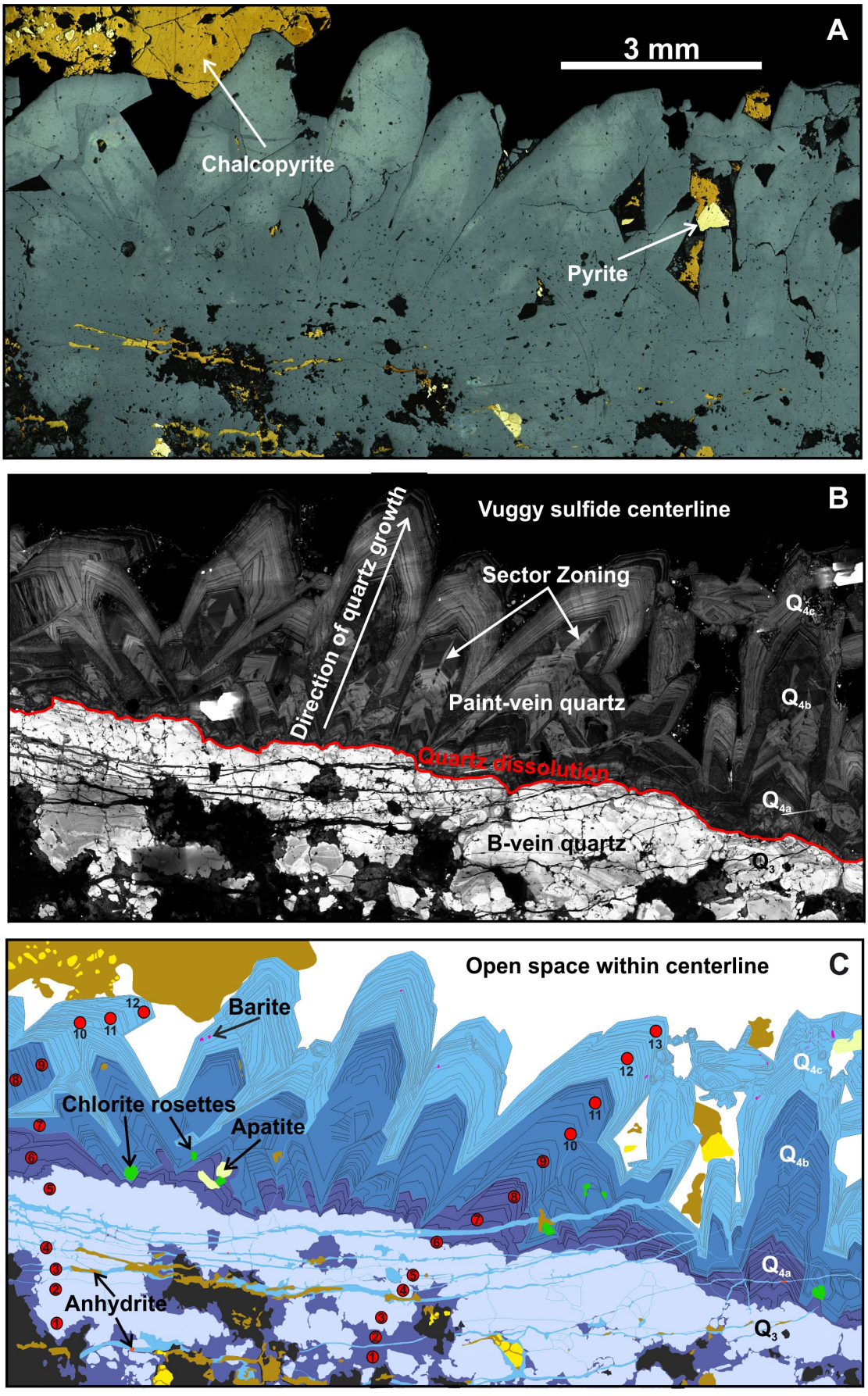
A
3 mm
Chalcopyrite
Pyrite
B
Vuggy sulfide centerline
Direction of quartz growth
Sector Zoning
Paint-vein quartz
Quartz dissolution
B-vein quartz
Q_{4c}
Q_{4b}
Q_{4a}
Q_3
C
Open space within centerline
Barite
Chlorite rosettes
Apatite
Anhydrite
Q_{4c}
Q_{4b}
Q_{4a}
Q_3

1310

Figure 7: Textural overview of reopened (A)B vein with vuggy sulfide centerline from the high-grade ore shell at Batu Hijau (SBD 95 601m). A) Reflected light image of euhedral Q_3 growing from the wall rock (bottom) to the center (top). Sulfides, mainly chalcopyrite with some pyrite, occur mainly in the open spaces or along cracks. Only few grains are within the quartz. B) Cathodoluminescence image of Q_{2-3} separated by a wavy dissolution front (red line) from the overgrowing Q_4. Bright luminescent spots represent anhydrite, apatite and barite inclusions. C) Simplified sketch of different Q_4 generations and distribution of sulfides and alteration minerals. B-vein quartz is pure and does not host any alteration or sulfide minerals. The earliest paint-vein quartz generation (Q_{4a}, purple) hosts anhydrite, apatite and barite crystals as well as chlorite rosettes but apparently no sulfides. The second generation (Q_{4b}, dark blue) hosts chalcopyrite grains, commonly along growth zones, and chlorite. The last generation (Q_{4c}, light blue) hosts most of the chalcopyrite and pyrite along cracks crosscutting all earlier quartz generations or in open spaces. Many rounded and small anhydrite, apatite and barite inclusions are present as well within the quartz and chalcopyrite. An evolution of the paint veins from chalcopyrite (potentially ± bornite) bearing over chalcopyrite-dominated to chalcopyrite + pyrite is visible here. The final stage of this evolution might be marked by the pyrite-dominated D veins. However, note that the distinction of different Q_4 generations is simplified and somewhat arbitrary here and many more sub-generations could be distinguished. The red dots represent LA-ICP-MS analyses along profiles crossing different quartz generations (Fig. 8).

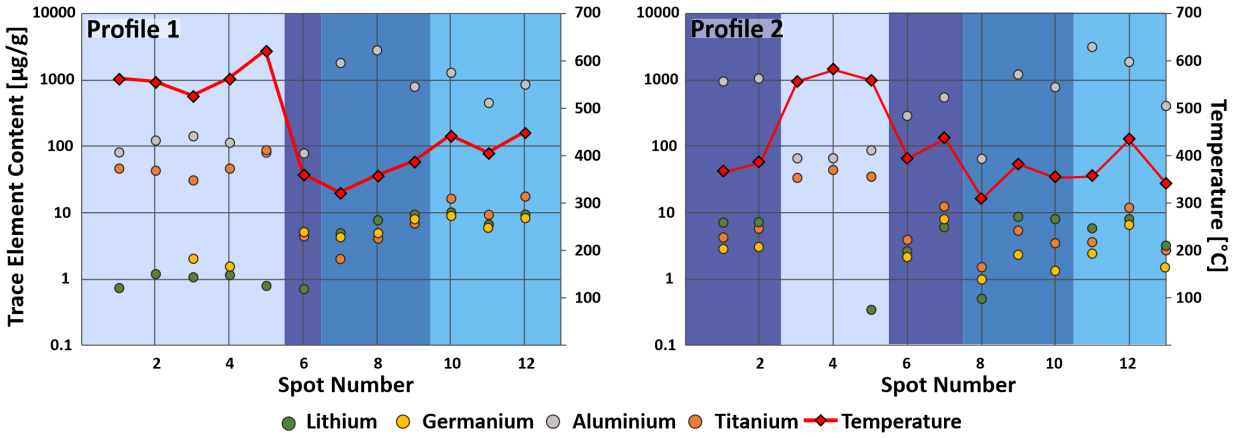

Figure 8: Spot analyses along profiles (Fig. 7C). Profile 1 includes 12 spot analyses (profile on the left in Fig. 7C) and profile 2 includes 13 spot analyses (right profile in Fig. 7C) crossing several quartz generations. Color-coding is the same as used in figure 6C. In general, all shown trace elements are significantly higher in the Q_4 generations, except for Ti which significantly decreases from up to 100 µg/g in the Q_{2-3} to below 15 µg/g in Q_{4a}. The temperature calculation is dependent on Ti content (Wark and Watson, 2006; Huang and Audétat, 2012).

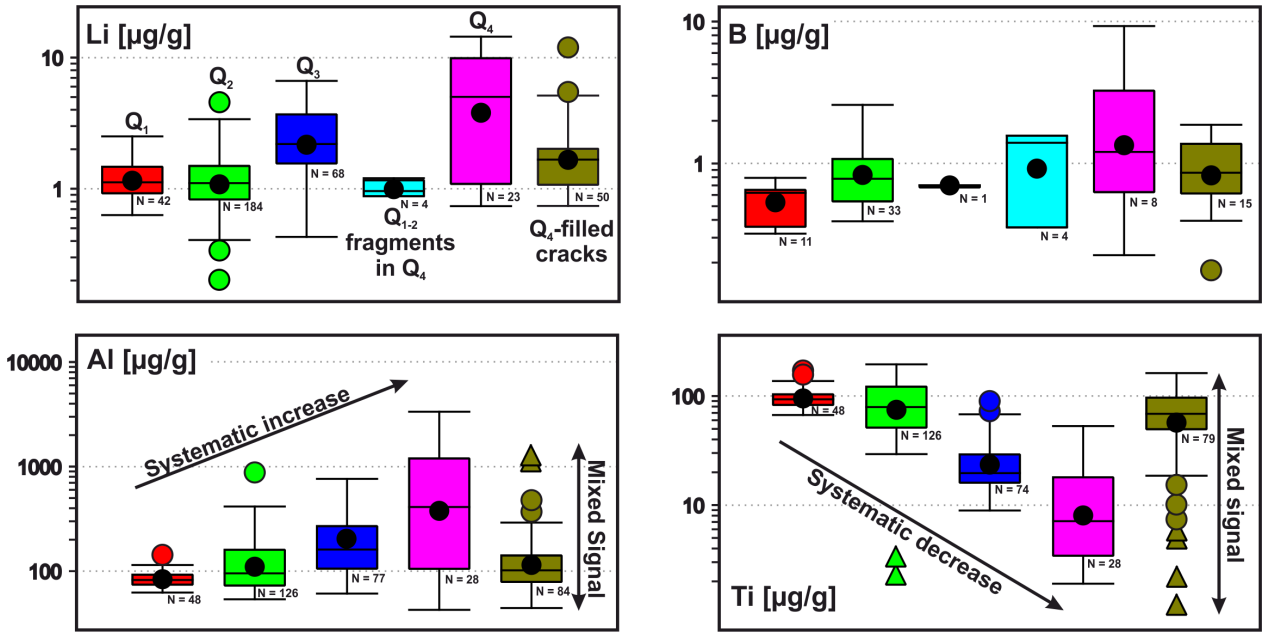

Figure 9: Box plots of selected trace elements in quartz (Q_1 to Q_4 represented by different colors). The lower whisker represents the first quartile, the bottom and top of the box the second and third quartile, respectively, and the upper whisker the fourth quartile of the data. The line and black dot within the boxes represent the median and average concentrations, respectively. Outliers are marked as colored circles (further away from the box than 1.5 x (value at the top of the box – value at the bottom of the box)) and far outliers are marked as colored triangles (further way from the box than 3.0 x (value at the top of the box – value at the bottom of the box)). Note that outliers have a pronounced effect on calculated averages compared to median values. All quartz generations representing different vein types partially overlap in their trace element concentrations. Nevertheless, on average Li, B, and Al concentrations increase from Q_1 to Q_4, whereas Ti decreases. Trace elements in Q_4 have the largest variations in composition, almost covering the total range of concentrations.

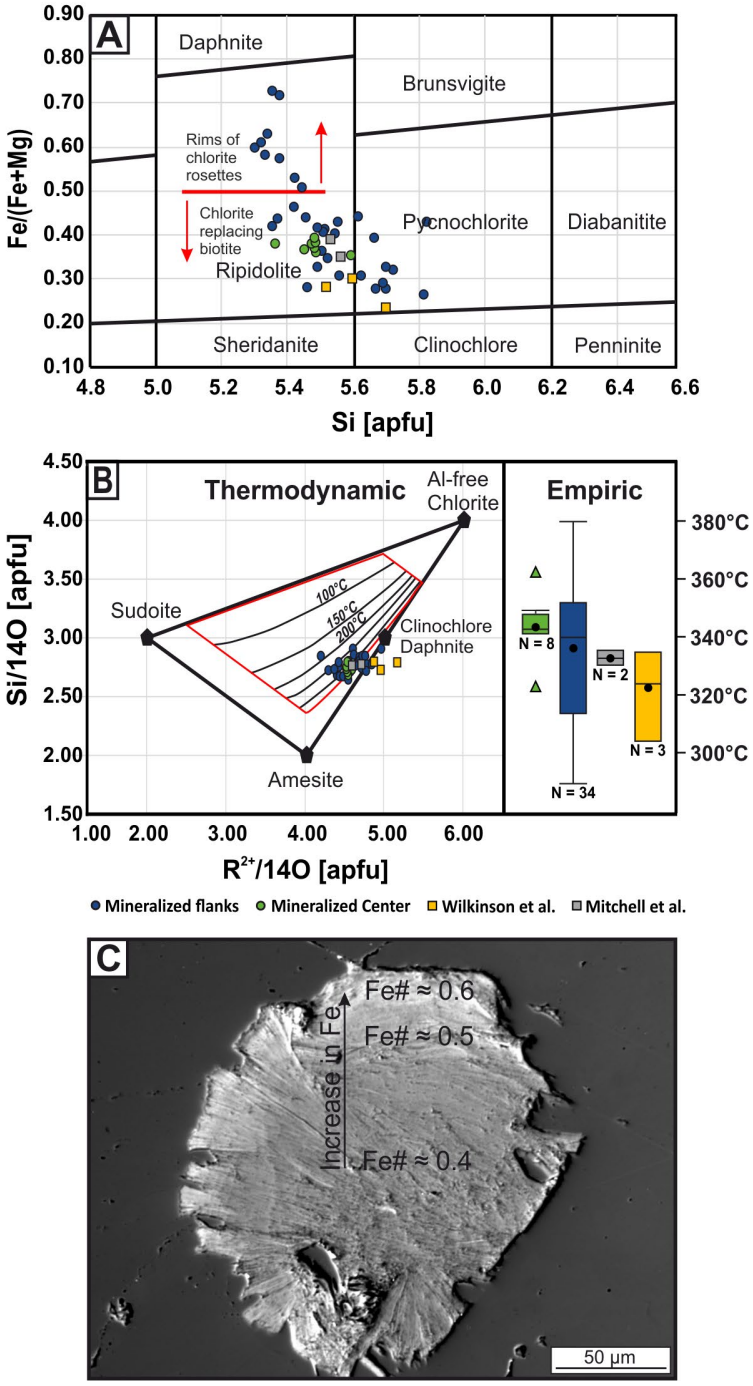

Figure 10: Results of chlorite analyses and comparison with EPMA data of chlorites from Batu Hijau obtained by Mitchell et al. (pers. commun., 1998) and Wilkinson et al. (2015). A) Classification scheme after Hey (1954) showing that most chlorites plot within the ripidolite and pycnochlorite field. B) T-R^{2+}-Si diagram of Bourdelle and Cathelineau (2015) predicting formation temperatures of chlorites based on a semi-empirical approach valid at low temperatures (<350 °C) and low pressures (< 3-4 kbar) considering chlorite-quartz equilibrium (Inoue et al., 2009; Bourdelle et al., 2013). Some points plot outside of the valid temperature field (red area), indicating that formation temperatures were higher than 350 °C or chlorite-quartz was not at equilibrium. However, most points (75%) plot between 300 and 350 °C, overlapping with results obtained by empirical calibrations (Jowett, 1991). C) Back-scattered electron image of chlorite rosette hosted by euhedral dull-luminescent paint-vein quartz (SBD 95 601m). Brighter rims indicate higher densities due to higher Fe contents.

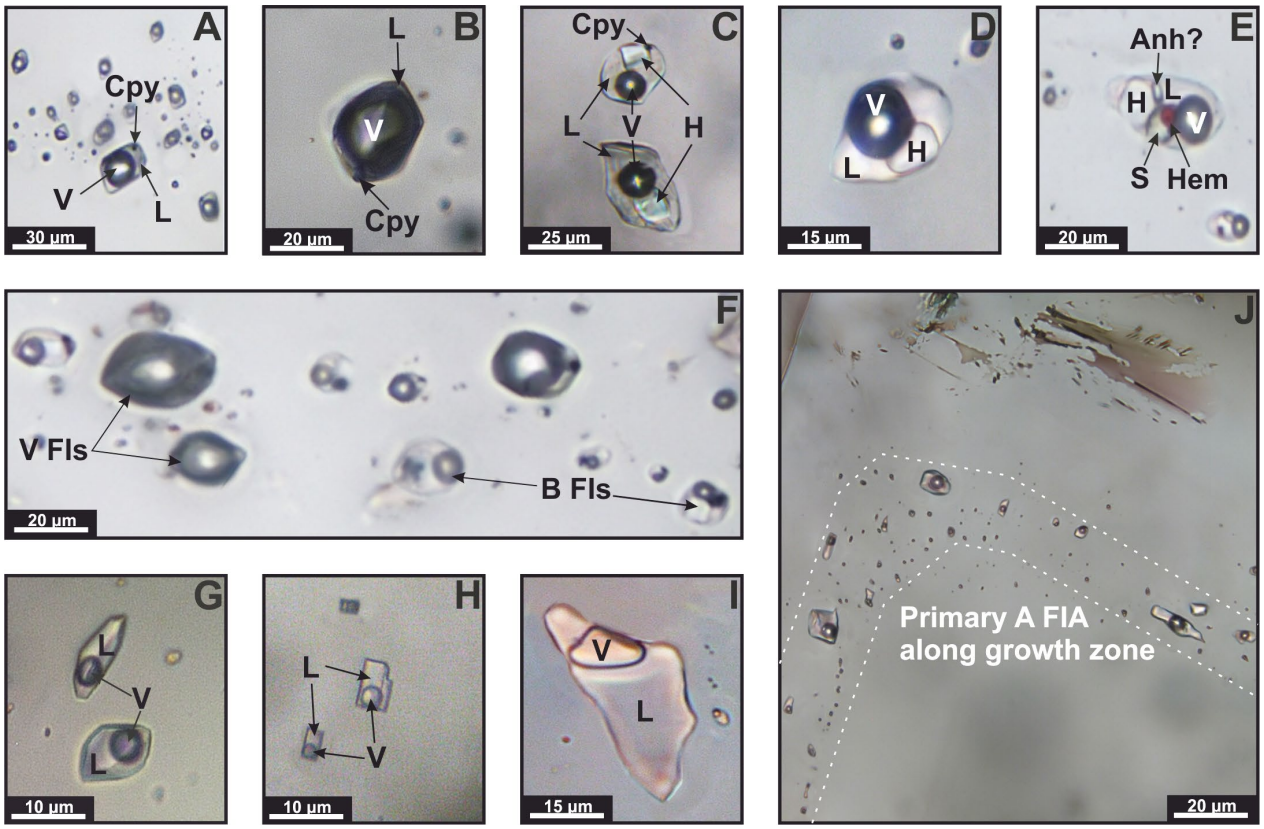

Figure 11: Different types of fluid inclusions hosted by veins. A) Two-phase intermediate density fluid inclusions with vapor (V) and liquid (L) filling the available space in equal proportions. Triangular opaque solids, probably chalcopyrite (Cpy), are present in almost all inclusions of this type. B) Vapor fluid inclusion filled mainly by vapor (~ 90 vol.%) and a thin rim of liquid wetting the fluid-crystal interface. Chalcopyrite daughter crystals are commonly present. C) B_1 fluid inclusions with small bubbles (~ 20 vol.%) and halite (H). D) High-temperature B_2 fluid inclusion with large vapor bubble (~ 30 vol.%). E) Complex B_3 fluid inclusion with several daughter crystals besides halite, such as sylvite (S), red flakes of hematite (Hem), and blueish, birefringent, commonly elongated, transparent anhydrite (Anh). Chalcopyrite is also present but not visible because it is covered by the vapor bubble. F) Boiling trail hosting brine and vapor fluid inclusions. G) Low-salinity aqueous fluid inclusions (AQ_2) within euhedral dull-luminescent paint-vein quartz. H) Rectangular aqueous fluid inclusions hosted by anhydrite in D-veins (AQ_3). I) Low-temperature, irregular and flat aqueous fluid inclusions may be associated with D-vein formation (AQ_3). J) Primary aqueous fluid inclusion assemblage along growth zone in euhedral paint-vein quartz (Q_4). This assemblage contains high-salinity aqueous inclusions (AQ_1) in which dissolution of hydrohalite was visible during freezing experiments. High- (AQ_1) and low-salinity aqueous fluid inclusions (AQ_2) are indistinguishable at room temperature.

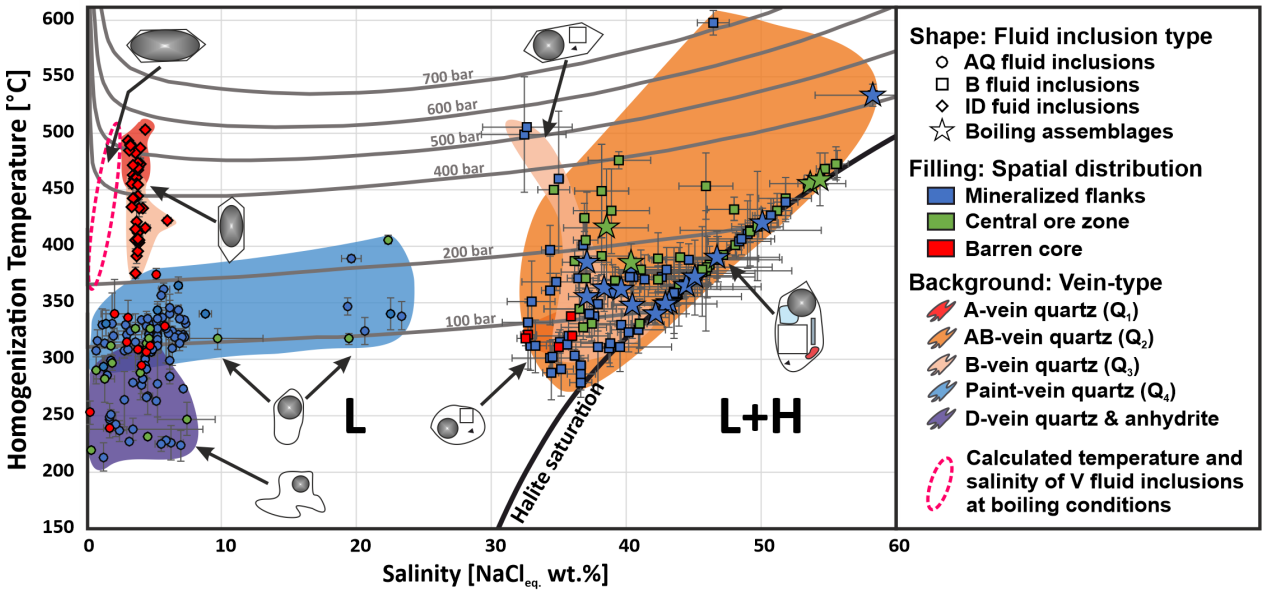

Figure 22: Microthermometry results of different fluid inclusion types within different parts and hydrothermal veins at Batu Hijau. Each dot represents a fluid inclusion assemblage with, on average, five individual fluid inclusions. Errors in homogenization temperature and salinity represent standard deviations between individual fluid inclusions within each assemblage. Due to the difficulty of conducting microthermometric experiments on vapor inclusions, salinities and homogenization temperatures were inferred from boiling assemblages using the SoWat software (Driesner, 2007; Driesner and Heinrich, 2007) and are shown with a dashed line. Fluid inclusion assemblages plotting on the halite saturation curve homogenized to the liquid phase by halite dissolution. Note that only intermediate density fluid inclusions are pressure corrected.

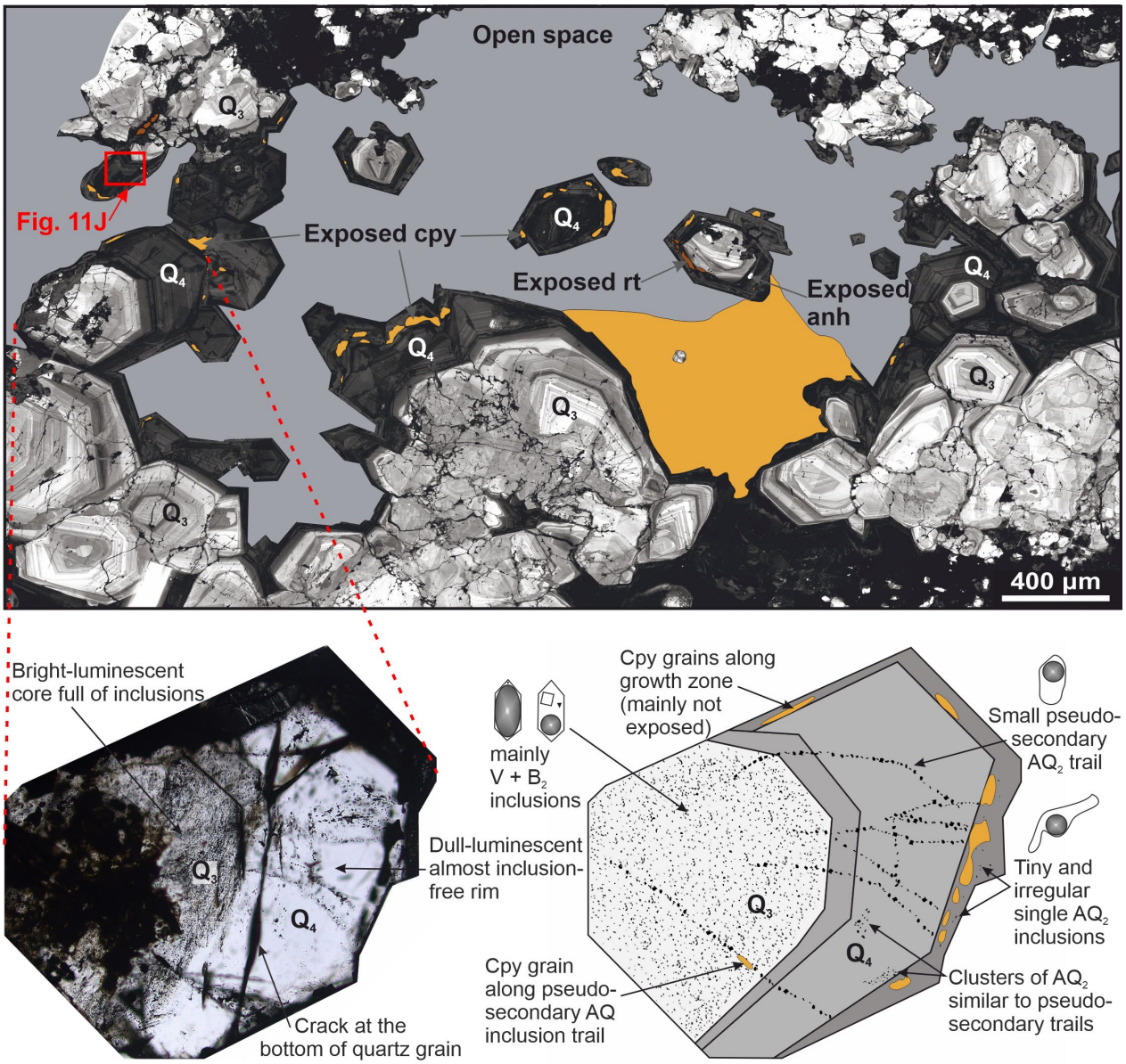

Figure 13: Cathodoluminescence image of paint vein intersecting B vein (top) and fluid inclusion distribution within a selected quartz grain (bottom; SBD 257 694m). Euhedral Q_4 overgrowing earlier euhedral Q_3, which shows several internal dissolution and re-precipitation textures. Chalcopyrite (cpy), anhydrite (anh) and rutile (rt) grains are exclusively hosted by Q_4, commonly along growth zones. Note that only exposed chalcopyrite and rutile are colored on the CL map. A transmitted light image and a schematic sketch of a selected quartz grain showing a bright-luminescent core and a dull-luminescent overgrowth with sulfide grains along a specific growth zone is shown in the lower part of the figure. The displayed distribution of fluid inclusions is typical for such composite grains, with countless B and V inclusions in the bright-luminescent core and an almost fluid inclusion free dull-luminescent quartz overgrowth. Fluid inclusions hosted by Q_4 are exclusively of the aqueous type occurring as pseudo-secondary trails that cut the bright-luminescent core and are truncated by the chalcopyrite-hosting growth zone. The outermost rim of the quartz crystal hosts tiny and irregular shaped AQ inclusions.

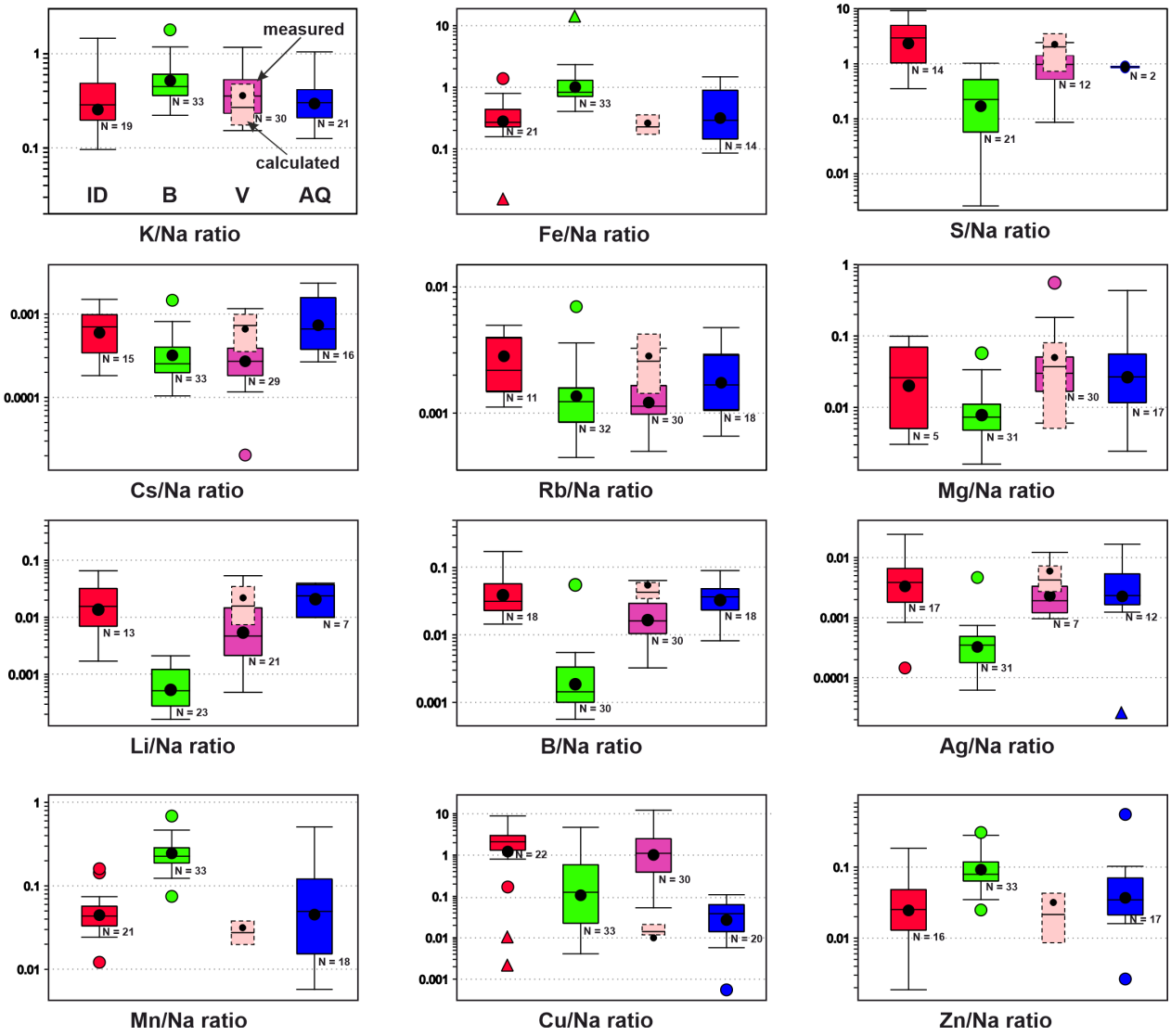

Figure 14: Box plots showing the element/Na mass ratios for different types of fluid inclusions (colors defined in the K/Na box). Each box represents the compositional range of FIAs of every fluid inclusion type. The total number of fluid inclusion assemblages (N) is indicated below each box. Both analyzed and calculated ratios for vapor inclusion are shown. Mass balance calculations are based on common boiling assemblages to correct for entrapped portions of brine following the procedure of Landtwing et al. (2010). In the same way, element/Na ratios were calculated for elements not analyzed in vapor inclusions. Calculated ratios are shown as a thinner pink box, commonly partially overlapping with the range of analyzed ratios in V FIAs. For explanation of Box and whisker plots see description of figure 9.

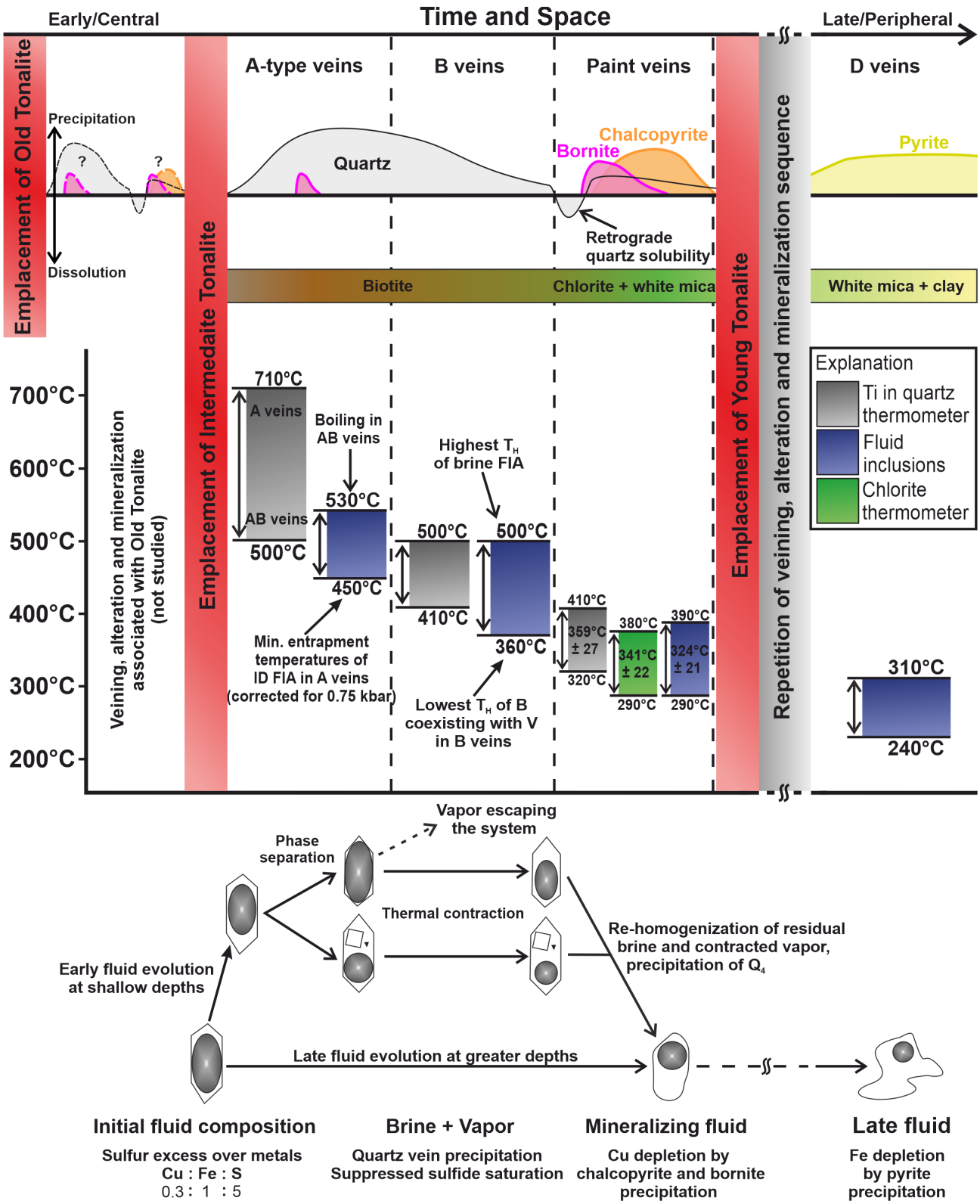

Figure 15: Summary showing from the top to the bottom the different veining stages, the precipitation or dissolution of selected hydrothermal minerals, the main alteration silicates in the host rock, the temperature evolution as documented by the various geothermometers, and a schematic evolution of the fluid with time based on fluid inclusion observations. Note that a similar veining, alteration and mineralization is expected to have occurred between the emplacement of the OT and IT but was not studied here due to the scarcity of samples that can be clearly identified as OT. Locally, high-temperature bornite formed during

quartz vein formation (Setyandhaka et al., 2008) but since this precipitation event was not documented within our sample collection, its exact timing relative to the different quartz-dominated vein types remains unknown. The lower part of the diagram summarises the sequence of fluid inclusions, interpreted in Figure 16A and particularly during the main mineralization stage shown in Figure 16B.

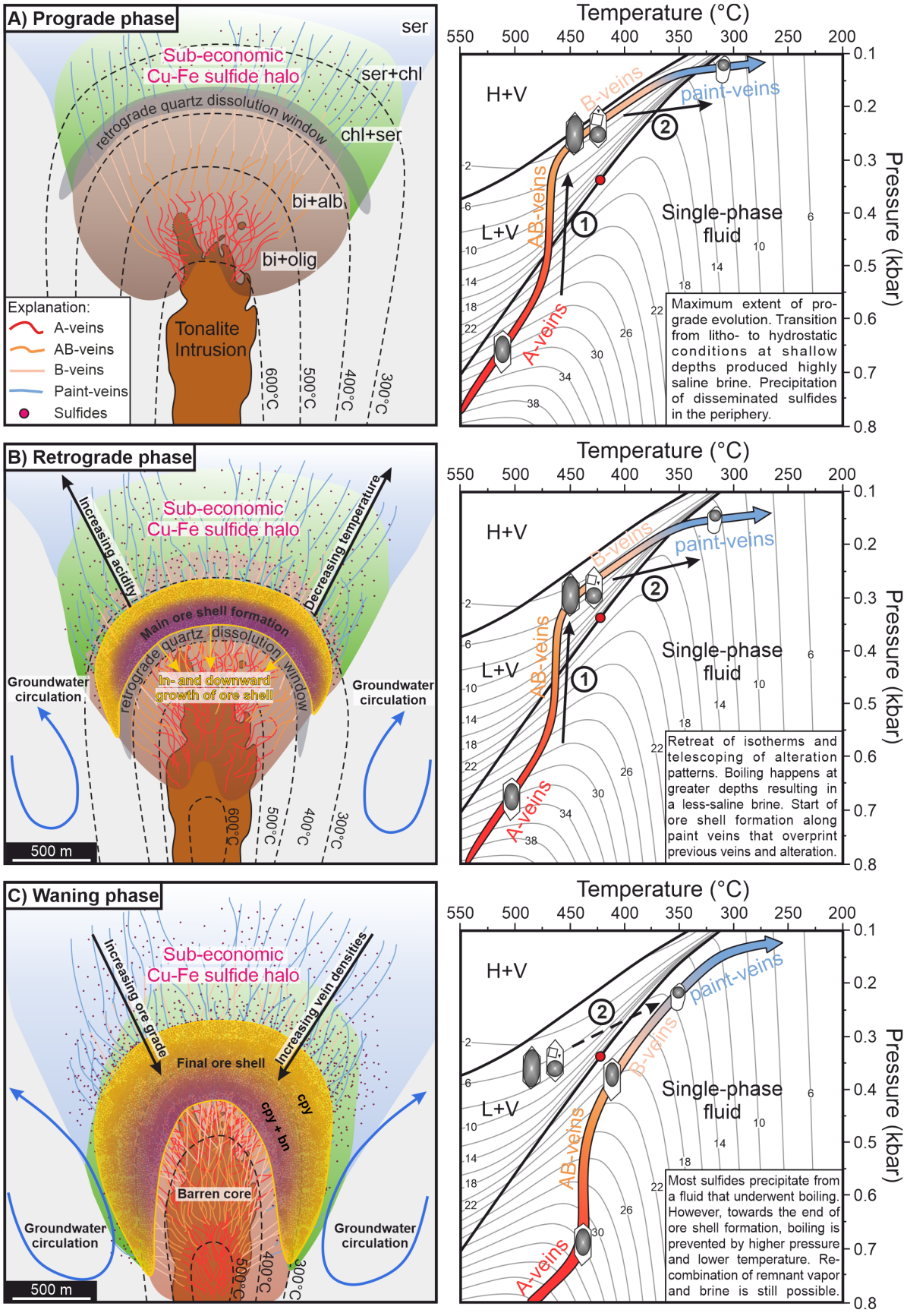
A) Prograde phase
ser
Sub-economic
Cu-Fe sulfide halo
ser+chl
retrograde quartz dissolution window
chl+ser
bi+alb
bi+olig
Tonalite
Intrusion
600°C
500°C
400°C
300°C
Explanation:
A-veins
AB-veins
B-veins
Paint-veins
Sulfides
Temperature (°C)
550 500 450 400 350 300 250 200
H+V
B-veins
paint-veins
L+V
AB-veins
A-veins
Single-phase
fluid
Maximum extent of pro-grade evolution. Transition from litho- to hydrostatic conditions at shallow depths produced highly saline brine. Precipitation of disseminated sulfides in the periphery.
Pressure (kbar)
0.1 0.2 0.3 0.4 0.5 0.6 0.7 0.8
B) Retrograde phase
Increasing acidity
Decreasing temperature
Sub-economic
Cu-Fe sulfide halo
Main ore shell formation
retrograde quartz dissolution window
In- and downward growth of ore shell
Groundwater circulation
Groundwater circulation
500 m
Retreat of isotherms and telescoping of alteration patterns. Boiling happens at greater depths resulting in a less-saline brine. Start of ore shell formation along paint veins that overprint previous veins and alteration.
C) Waning phase
Increasing ore grade
Increasing vein densities
Sub-economic
Cu-Fe sulfide halo
Final ore shell
cpy
cpy + bn
Barren core
Groundwater circulation
Groundwater circulation
500 m
Most sulfides precipitate from a fluid that underwent boiling. However, towards the end of ore shell formation, boiling is prevented by higher pressure and lower temperature. Re-combination of remnant vapor and brine is still possible.

Figure 36: Hydrothermal evolution at Batu Hijau as schematic sketch in the left column and fluid evolution as function of temperature and pressure in the right column. Quartz solubility contours in mmol/kg of fluid are taken from Monecke et al. (2018), the red dot represents the critical point of a fluid containing 5 wt.% NaCl. Lateral zonation of propylitic alteration is not shown for simplicity. The shown schematic model involves a progressive telescoping process during retreat of isotherms producing overprinting alteration, crosscutting vein types and mineralization with the associated evolution of the fluid as recorded by fluid inclusions. Arrows labeled 1 and 2 represent phase separation and re-homogenization of previously separated brine and vapor, respectively. Sulfide precipitation starts early in the hydrothermal evolution but distal from the present day ore shell, producing the wide halo of sub-economically mineralized rocks around Batu Hijau as shown in part A). By reduction of the volume and stabilization of the isotherms at depth, sulfide precipitation is more focused, which led to ore shell formation. Part B) shows the initiation of ore shell formation during the retrograde stage of the system. The major part of ore shell forms during the retrograde phase by transient stabilization of the in- and downward retracting mineralization front. The final shape of the ore shell mimics the positions of the 350°C isotherm with time and is shown in part C). During the waning stage only minor amounts of Cu will be added to or potentially even removed from the system. Ground water convection through the porous volcanoclastic host rocks effectively cools the hydrothermal systems and produces steep isotherms defining the ultimate shape of the ore shell (Weis, 2015).

Table 2: Characteristics of vein types and associated alteration at Batu Hijau.

Vein Type	Mineralogy	Alteration Halo	Thickness	Geometry	CL intensity of quartz	Fluid Inclusions	Pressure regime	References
A	Qtz + mag ± bi ± olig ± anh Cpy + bn	Bi + olig ± mag	< 1.5 cm	Irregular, wavy	Bright-luminescent, anhedral granular	ID in barren core, less commonly V and rarely B	Lithostatic	1), 2), 3), 4), this study
AB	Qtz ± mag ± bi/chl ± alb ± anh Cpy ± bn	Alb ± bi	1 – 5 cm	Regular, less wavy	Bright-luminescent, an- to subhedral, granular to prismatic	ID in barren core, B + V in the mineralized zone (boiling)	Lithostatic	2), 3), 4), this study
B	Qtz ± chl ± alb ± anh Cpy ± bn (± mo, barren core)	Alb ± chl	< 2.5 cm	Regular, straight, centerline	Medium-luminescent, comb-like, euhedral with oscillatory growth zoning	ID in barren core, B + V in the mineralized zone (boiling)	Litho- to hydro- or vaporstatic	1), 2), 3), 4), this study
Paint (C)	Chl + ser + rt ± qtz ± anh ± ba ± tit ± cal ± ap Cpy ± bn or cpy ± py or py ± cpy	Chl + ser + rt + cal ± anh ± hem	< 0.1 cm, in rare cases up to 1.0 cm	Indistinct, irregular , vuggy	Dull-luminescent, comb-like, anhedral to euhedral with oscillatory growth zoning	Small rounded A	Hydro- to vaporstatic	this study (4)
D	Py ± cpy ± ser ± anh	Ser + py	0.5 - 2 cm	Regular, straight	Dull-luminescent fragments, euhedral	Irregular A in qtz and rectangular A in anh	Hydro- to vaporstatic	1), 2), 3), 4), this study

Mineral abbreviations: alb – albite, anh – anhydrite, ap – apatite, ba – barite, bi – biotite, bn – bornite, cal – calcite, chl – chlorite, cpy – chalcopyrite, hem – hematite, mag – magnetite, mo – molybdenite, olig – oligoclase, py – pyrite, qtz – quartz, rt – rutile, ser – white mica, tit- titanite.

Abbreviations for vein and fluid inclusion types as explained in text.

References: 1) Clode et al., 1999, 2) Garwin, 2000, 3) Arif and Baker, 2004, 4) Idrus et al., 2009

1448

1449 Table 3: Characteristics and compositions of the different quartz generations.

Quartz Gen.	Vein Type	CL characteristics	Habitus	Trace Element Concentrations			
				Li	B	Al	Ti
Q_1	Am, A	Bright luminescent, wavy growth zonation rarely visible	Anhedral, sugary mosaic texture	0.6 - 2.5 Ø: 1.2	0.3 - 0.8 Ø: 0.5	62 - 114 Ø: 84	67 - 144 Ø: 95
Q_2	AB	Bright luminescent, wavy growth zonation commonly present	An- to subhedral, sugary mosaic texture	0.4 - 3.4 Ø: 1.1	0.4 - 2.6 Ø: 0.8	54 - 415 Ø: 111	29 - 159 Ø: 75
Q_3	B	Medium luminescent, sharp euhedral growth zoning	Prismatic, euhedral growth zoning, comb-texture	0.4 - 6.6 Ø: 2.2	0.7 - 0.7 Ø: 0.7	61 - 763 Ø: 161	9 - 68 Ø: 24
Q_4 (Q_5?)	Paint, D	Dull luminescent, sharp euhedral growth zoning	Like Q_3 in open spaces, anhedral in cracks	0.7 - 14.4 Ø: 3.8	0.2 - 9.3 Ø: 1.3	43 - 3348 Ø: 377	2 - 53 Ø: 8

1450